AIAA Aviation Forum and ASCEND co-located Conference Proceedings
29 July - 2 August 2024, Las Vegas, Nevada
AIAA AVIATION FORUM AND ASCEND 2024
10.2514/6.2024-3793

Improved Delayed Detached Eddy Simulation of Co-Flow Jet Flow Control with Enthalpy Effects

B. McBreen,* Y.-C. Yang,† G.-C. Zha‡
Dept. of Mechanical and Aerospace Engineering
University of Miami, Coral Gables, Florida 33146
E-mail: gzha@miami.edu

Abstract

This paper investigates the effects of high enthalpy flow associated with Co-Flow Jet (CFJ) active flow control, using 3D Improved Delayed Detached Eddy Simulation (IDDES). The simulation is conducted using FASIP, an in-house CFD solver. The spatially filtered Navier-Stokes equations are solved using a fifth-order WENO reconstruction scheme for the inviscid fluxes and a fourth order central differencing scheme for the viscous fluxes. The IDDES model of Spalart et al. is adopted. While past studies of CFJ active flow control assume a zero total enthalpy increase across the fluidic actuator driving the CFJ flow ("Cold Jet CFJ"), this study accounts for the increase in total enthalpy due to the total pressure ratio across the actuator ("Hot Jet CFJ"). The airfoil studied is a CFJ6421-SST150-SUC247-INJ152 at an angle of attack $\alpha = 65°$ and a jet momentum coefficient $C_\mu = 2.5$. With an idealized compressor assuming constant total enthalpy, this CFJ airfoil achieves a Super-Lift Coefficient of $C_L = 9.58$. With a compressor efficiency $\eta = 70\%$, the CFJ injection jet reaches an equilibrium injection total temperature $T_{02}/T_{0_\infty} = 1.196$, and the lift coefficient improves 4.8%, to $C_L = 10.04$. This greater lift coefficient comes at the cost of a higher drag and power required. Considering the high total enthalpy jet at $\eta = 70\%$, the corrected aerodynamic efficiency drops from $(C_L/C_D)_c = 1.885$ to 1.784. Irreversible losses in the high pressure gradient regions of the injection jet and shear mixing layer make up about 5.7% of the system efficiency loss. These differences are attributed to the additional total enthalpy of the CFJ injection flow, which causes much greater turbulence generation within the injection duct, leading to stronger mixing in the wall jet's shear layer, transferring energy and momentum to the main flow. The "Hot Jet" case shows complex, unsteady flow structures with substantially enhanced streamwise vortex structures, which are not present in the "Cold Jet" case. The turbulent nature of the high enthalpy injection jet flow augments the mixing across the CFJ's shear layer. This CFJ airfoil has been demonstrated to be a highly effective flow control technique; implementation of the "Hot Jet" boundary condition to the simulation proves that the CFJ's lift coefficient could be even higher than previously reported. On the other hand, it also shows that the power required is somewhat higher than previously reported.

Nomenclature

AoA, α	Angle of Attack
AFC	Active Flow Control
CFJ	Co-Flow Jet
$FASIP$	Flow-Acoustics-Structure Interaction Package
SLC	Super-Lift Coefficient
TKE	Turbulent Kinetic Energy

* Ph.D.
† Ph.D.
‡ Professor, AIAA Associate Fellow

C_L	Lift coefficient
C_D	Drag coefficient
C_μ	Jet momentum coefficient, $C_\mu = \frac{\dot{m}V_j}{\frac{1}{2}\rho_\infty {V_\infty}^2 S}$
$C_{L_{max}}$	Maximum lift coefficient
$(C_L/C_D)_c$	Aerodynamic efficiency corrected for CFJ airfoil, $\frac{L}{D+P/V_\infty}$
P	CFJ pumping power consumption, $P = \frac{\dot{m}C_pT_{t2}}{\eta}(\Gamma^{\frac{\gamma-1}{\gamma}} - 1)$
P_c	Power coefficient, $P_c = \frac{P}{\frac{1}{2}\rho_\infty V_\infty^3 S}$
C, L	Airfoil chord, reference length
Re	Reynolds number
Ma	Mach number
ρ_∞	Freestream density
V_∞	Freestream velocity
γ	Air specific heats ratio
R	Boltzmann gas constant
$\dot{m}$	Mass flow across the pump
T_t	Total temperature
P_t	Total pressure
H_t	Total enthalpy, c_pT_t
S	Entropy
PTR, PR	Total pressure ratio, Γ
TTR	Total temperature ratio
η	CFJ pumping system efficiency
ω_z	Spanwise Vorticity
ω_s	Streamwise Vorticity
ω_n	Normal Vorticity
St	Strouhal Number, fL/U
G	Gortler Parameter
R	Streamline curvature radius
θ	Boundary layer momentum thickness
β	Spanwise wavenumber
U_s	Max. velocity in wall jet
λ	Wavelength

1 Introduction

Since the dawn of aerodynamics, engineers have sought to expand the operational limits of aircraft, flying farther, higher, and with heavier payloads. The airfoil, a critical component enabling flight, has been the focus of extensive optimization to enhance its lift and efficiency. Innovations such as flaps and slats as passive high lift devices marked significant progress in classical airfoil design, further improving performance. The next frontier in advancing airfoil capabilities lies in Active Flow Control (AFC) [1, 2].

Co-Flow Jet (CFJ) is a very promising promising AFC technology. Airfoils incorporating CFJ AFC have been shown to produce greater maximum lift coefficients [3, 4, 5, 6, 7], and higher cruise efficiencies [6, 7, 8, 9, 10, 11, 12, 13, 14] than conventional or flapped airfoil systems, and have demonstrated other unique abilities such as

reducing power required for VTOL flight [15], preventing stall [3, 4, 16, 17, 18], and improving the power output of wind turbines [19, 20, 21, 22]. CFJ airfoils, which integrate tangential injection and streamwise suction slots to the airfoil, have demonstrated high control authority and energy efficiency. These characteristics make CFJ technology highly effective for both takeoff and cruise configurations. Despite these advancements, there is a lack of deep understanding of the fundamental physics governing this flow control technique.

Previous numerical study of CFJ has assumed an idealized fluidic actuator with constant total temperature, with constant total enthalpy across the fluidic actuator. These studies have provided valuable insights into the basic mechanisms and benefits of CFJ technology, demonstrating significant improvements in aerodynamic performance. However, the assumption of constant total enthalpy does not fully capture the realistic operating conditions of CFJ systems, where the injection jet has a higher total temperature due to the energy input from the micro-compressor, especially as we study high power applications of the CFJ.

Previous numerical study has assessed the power required of the CFJ by simulating the flow without considering a change in total enthalpy, then dividing the calculated power required by the efficiency of the micro-compressor actuators to determine the actual power required. This approach is analogous to system-level aircraft design, which defines power required as $P_{req} = DV$, where D is the drag and V is the aircraft flight velocity. The actual power consumed by the aircraft will be $P_{act} = P_{req}/\eta$, where η is the propulsor efficiency. The Total Pressure Ratio (PTR) across the propellers is generally a few percent, and the total enthalpy rise is similarly small. Thus the enthalpy effect is usually not considered in system-level aircraft design. Similarly, past CFJ studies have found that the PTR is low for cruise condition implementations. For cruise Mach numbers up to $Ma = 0.3$, the PR is 1.015–1.06 [14, 23]. The total enthalpy increment across the CFJ actuator is in the same order of magnitude of the total pressure increment, and has a minimal on the flow field. The effect of the total enthalpy has been neglected in previous studies for convenience. However, some applications of CFJ can result in a PR in the order of 10–20%, such as cruise at Mach 0.4–0.72 [14, 23, 24], and low speed, high angle of attack applications [4, 18, 25]. In these cases, the entropy generation may be significant. It is thus important to study the impact of an accurate jet total enthalpy to better understand the physics related to the more realistic process.

This study aims to fill the gap in the current research by investigating the effects of Hot Jet CFJ. Specifically, the study examines how varying the total temperature of the jet influences turbulence generation, energy transfer, mixing, lift and drag performance, and power requirements. By providing a more realistic representation of CFJ flow, this research seeks to enhance our understanding of CFJ in practical applications.

1.1 The Co-Flow Jet Active Flow Control Airfoil

The Co-Flow Jet airfoil has a tangential injection slot near the leading edge (LE) of the airfoil's suction surface and a streamwise suction slot near the trailing edge (TE). Flow is ingested into the airfoil through the suction slot, pressurized and energized by a micro-compressor inside the airfoil, then injected near the leading edge through the injection slot. The injection jet flow profile is characteristic of a a wall jet [8]. Energy and momentum are transferred from the micro-compressor to the main flow across the turbulent wall jet shear layer [3].

Co-Flow Jet active flow control has been shown to have high control authority effectiveness, and high energy efficiency at both high lift takeoff and low lift cruise configurations [6, 7, 8, 9, 10, 11, 12, 13, 14]. The CFJ airfoil's performance and capabilities are derived from its design. The CFJ is a self contained zero-net-mass-flux system. A micro-compressor fluidic actuator powers the system with high jet momentum and high energy conversion efficiency. The jet slots are strategically positioned such that the suction slot draws flow from a high pressure region, and the injection slot injects flow into a low pressure region, allowing the pump to operate at a low pressure ratio, and low required power.

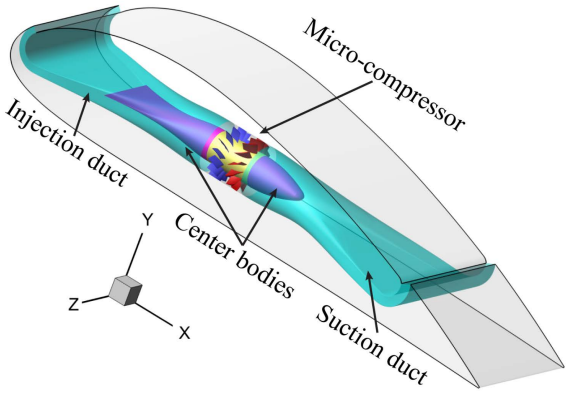

Figure 1: Schematic of components within CFJ airfoil.

The CFJ "strength" is modulated by C_μ, the injection jet momentum coefficient. In most prior CFJ studies using FASIP, the micro-compressor is not directly simulated, but a pair of inlet/outlet boundary conditions are used to imitate the pump's effect on the flow. To achieve zero net mass flux, the mass flow exiting the injection slot equals the mass flow entering the suction slot, i.e. $\dot{m}_{inj} = \dot{m}_{suc}$. The prescribed jet momentum coefficient, C_μ, is achieved by iterating the injection boundary total pressure. The injection and suction mass flow rates are then matched by adjusting the suction cavity static pressure. The iterative process is conducted throughout the simulation until the specified momentum coefficient is reached and the injection and suction mass flow match within an acceptable tolerance, typically $\epsilon = 1\%$. In previous CFJ studies, the injection and suction boundary total temperatures has been assumed to be equal to simplify the boundary condition implementation. This assumption has been shown to be valid for many previous CFJ studies because of the very low PTR required to drive the CFJ fluidic actuator [6, 7, 10, 26].

For simulations of the CFJ airfoil at very high angles of attack, the constant Total Temperature Ratio (TTR) assumption is invalid. Cold Jet 3D IDDES simulation of the same CFJ airfoil configuration studied in this paper found that the total pressure ratio across the pump is 1.076 [3]. Since the pump is a non-isentropic process, the TTR should be 1.030, a number too large to ignore. In this study, the CFJ pumping efficiency is set to 70% to conservatively reflect estimated compressor efficiency [14, 25]. Figure 2 shows an example compressor map of a recently published CFJ micro-compressor design. A lower efficiency also increases the total enthalpy difference, and the increases the temperature of the jet flow.

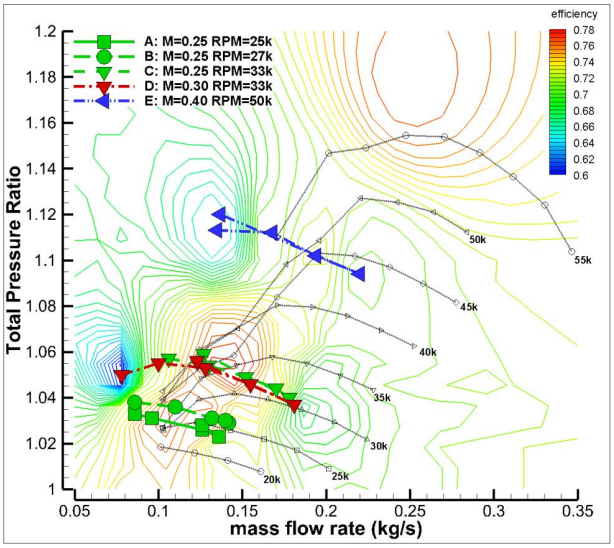

Figure 2: CFJ G8 compressor map [14]

Yang and Zha first identified that a CFJ airfoil can sustain lifting flow at AoA up to 70° without stall [4], generating exceedingly high lift coefficients. For the CFJ6421 airfoil, lift coefficients greater than 7.6 are termed a *Super-Lift Coefficient* (SLC) [4]. Their 2017 paper finds a $C_{L\ max} = 12.6$ at $\alpha = 70°$. In a follow on study with the airfoil modified to have a 30% larger injection slot, McBreen et. al. find a $C_{L\ max} = 16.0$ at $\alpha = 65°$ [17]. The CFJ6421 airfoil was also shown to generate a SLC by the wind tunnel testing, reaching a max lift coefficient of 8.6 [5].

2 Numerical Algorithms

2.1 Governing Equations

The spatially filtered Navier-Stokes governing equations in generalized coordinates are expressed as:

$$\frac{\partial \mathbf{Q}}{\partial t}+\frac{\partial \mathbf{E}}{\partial \xi}+\frac{\partial \mathbf{F}}{\partial \eta}+\frac{\partial \mathbf{G}}{\partial \zeta}=\frac{1}{Re}\left(\frac{\partial \mathbf{E}_v}{\partial \xi}+\frac{\partial \mathbf{F}_v}{\partial \eta}+\frac{\partial \mathbf{G}_v}{\partial \zeta}+\mathbf{S}\right) \tag{1}$$

where Re is the Reynolds number. The equations are normalized based on airfoil chord L, freestream density ρ_∞, and freestream velocity U_∞.

The conservative variable vector $\mathbf{Q}$, the inviscid flux vectors $\mathbf{E}$, $\mathbf{F}$, $\mathbf{G}$, the viscous flux $\mathbf{E_v}$, $\mathbf{F_v}$, $\mathbf{G_v}$ and the source term vector $\mathbf{S}$ are expressed as

$$\mathbf{Q}=\frac{1}{J}\begin{pmatrix}\bar{\rho}\\ \bar{\rho}\tilde{u}\\ \bar{\rho}\tilde{v}\\ \bar{\rho}\tilde{w}\\ \bar{\rho}\tilde{e}\\ \bar{\rho}\tilde{\nu}_t\end{pmatrix},\mathbf{E}=\begin{pmatrix}\bar{\rho}U\\ \bar{\rho}\tilde{u}U+l_x\bar{p}\\ \bar{\rho}\tilde{v}U+l_y\bar{p}\\ \bar{\rho}\tilde{w}U+l_z\bar{p}\\ \left(\bar{\rho}\tilde{e}+\bar{p}\right)U-l_t\bar{p}\\ \bar{\rho}\tilde{\nu}U\end{pmatrix},\mathbf{F}=\begin{pmatrix}\bar{\rho}V\\ \bar{\rho}\tilde{u}V+m_x\bar{p}\\ \bar{\rho}\tilde{v}V+m_y\bar{p}\\ \bar{\rho}\tilde{w}V+m_z\bar{p}\\ \left(\bar{\rho}\tilde{e}+\bar{p}\right)V-m_t\bar{p}\\ \bar{\rho}\tilde{\nu}V\end{pmatrix},\mathbf{G}=\begin{pmatrix}\bar{\rho}W\\ \bar{\rho}\tilde{u}W+n_x\bar{p}\\ \bar{\rho}\tilde{v}W+n_y\bar{p}\\ \bar{\rho}\tilde{w}W+n_z\bar{p}\\ \left(\bar{\rho}\tilde{e}+\bar{p}\right)W-n_t\bar{p}\\ \bar{\rho}\tilde{\nu}W\end{pmatrix} \tag{2}$$

$$\mathbf{E_v}=\begin{pmatrix}0\\ l_k\bar{\tau}_{xk}\\ l_k\bar{\tau}_{yk}\\ l_k\bar{\tau}_{zk}\\ l_k\left(\tilde{u}_i\bar{\tau}_{ki}-\bar{q}_k\right)\\ \frac{\bar{\rho}}{\sigma}\left(\nu+\tilde{\nu}\right)\left(\mathbf{l}\bullet\nabla\tilde{\nu}\right)\end{pmatrix},\mathbf{F_v}=\begin{pmatrix}0\\ m_k\bar{\tau}u_{xk}\\ m_k\bar{\tau}_{yk}\\ m_k\bar{\tau}u_{zk}\\ m_k\left(\tilde{u}_i\bar{\tau}_{ki}-\bar{q}_k\right)\\ \frac{\bar{\rho}}{\sigma}\left(\nu+\tilde{\nu}\right)\left(\mathbf{m}\bullet\nabla\tilde{\nu}\right)\end{pmatrix},\mathbf{G_v}=\begin{pmatrix}0\\ n_k\bar{\tau}_{xk}\\ n_k\bar{\tau}_{yk}\\ n_k\bar{\tau}_{zk}\\ n_k\left(\tilde{u}_i\bar{\tau}_{ki}-\bar{q}_k\right)\\ \frac{\bar{\rho}}{\sigma}\left(\nu+\tilde{\nu}\right)\left(\mathbf{n}\bullet\nabla\tilde{\nu}\right)\end{pmatrix} \tag{3}$$

$$\mathbf{S}=\frac{1}{J}\begin{pmatrix}0\\ 0\\ 0\\ 0\\ 0\\ S_\nu\end{pmatrix} \tag{4}$$

where ρ is the density, p is the static pressure, and e is the total energy per unit mass. The overbar term denotes a regular filtered variable in the LES region,or a Reynolds-averaged value in the RANS region. And the tilde symbol is used to denote the Favre filtered variable. ν is kinematic viscosity and $\tilde{\nu}$ is the working variable related to eddy viscosity in S-A and IDDES turbulence one equation model [27]. U, V and W are the contravariant velocities in ξ, η, ζ directions, and defined as

$$\begin{aligned}U&=l_t+\mathbf{l}\bullet\mathbf{V}=l_t+l_x\tilde{u}+l_y\tilde{v}+l_z\tilde{w}\\ V&=m_t+\mathbf{m}\bullet\mathbf{V}=m_t+m_x\tilde{u}+m_y\tilde{v}+m_z\tilde{w}\\ W&=n_t+\mathbf{n}\bullet\mathbf{V}=n_t+n_x\tilde{u}+n_y\tilde{v}+n_z\tilde{w}\end{aligned} \tag{5}$$

J is the Jacobian of the coordinate transformation. l_t, m_t and n_t are the components of the interface contravariant velocity of the grid in ξ, η and ζ directions respectively. $\mathbf{l}$, $\mathbf{m}$ and $\mathbf{n}$ denote the normal vectors located at the centers of ξ, η and ζ interfaces of the control volume with their magnitudes equal to the surface areas and pointing to the directions of increasing ξ, η and ζ.

$$\mathbf{l} = \frac{\nabla\xi}{J},\ \mathbf{m} = \frac{\nabla\eta}{J},\ \mathbf{n} = \frac{\nabla\zeta}{J} \tag{6}$$

$$l_t = \frac{\xi_t}{J},\ m_t = \frac{\eta_t}{J},\ n_t = \frac{\zeta_t}{J} \tag{7}$$

In the generalized coordinates, $\Delta\xi = \Delta\eta = \Delta\zeta = 1$. Since the DES-family approach is based on S-A model, the formulations of the original S-A model are give below. The source term S_ν from the S-A model in Eq. 4, is given by

$$\begin{aligned} S_\nu = \bar{\rho}C_{b1}\left(1-f_{t2}\right)\tilde{S}\tilde{\nu} + \tfrac{1}{Re}\left[-\bar{\rho}\left(C_{w1}f_w - \tfrac{C_{b1}}{\kappa^2}f_{t2}\right)\left(\tfrac{\tilde{\nu}}{d}\right)^2\right. \\ \left. +\tfrac{\bar{\rho}}{\sigma}C_{b2}\left(\nabla\tilde{\nu}\right)^2 - \tfrac{1}{\sigma}\left(\nu+\tilde{\nu}\right)\nabla\tilde{\nu}\bullet\nabla\bar{\rho}\right] + Re\left[\bar{\rho}f_{t1}\left(\Delta q\right)^2\right] \end{aligned} \tag{8}$$

where

$$\chi = \frac{\tilde{\nu}}{\nu}, \quad f_{v1} = \frac{\chi^3}{\chi^3 + c_{v1}^3}, \quad f_{v2} = 1 - \frac{\chi}{1+\chi f_{v1}}, \quad f_{t1} = C_{t1}g_t exp\left[-C_{t2}\frac{\omega_t^2}{\Delta U^2}\left(d^2 + g_t^2 d_t^2\right)\right] \tag{9}$$

$$f_{t2} = C_{t3}exp\left(-C_{t4}\chi^2\right), \quad f_w = g(\frac{1+c_{w3}^6}{g^6+c_{w3}^6})^{1/6}, \quad g = r + c_{w2}(r^6 - r) \tag{10}$$

$$g_t = min\left(0.1, \frac{\Delta q}{\omega_t \Delta x_t}\right), \quad \tilde{S} = S + \frac{\tilde{\nu}}{k^2 d^2 R_e}f_{v2}, \quad r = \frac{\tilde{\nu}}{\tilde{S}k^2 d^2 R_e} \tag{11}$$

ω_t is the wall vorticity at the wall boundary layer trip location, d is the distance to the closest wall, d_t is the distance of the field point to the trip location, Δq is the difference of the velocities between the field point and the trip location, Δx_t is the grid spacing along the wall at the trip location. The values of the coefficients are: $c_{b1} = 0.1355, c_{b2} = 0.622, \sigma = \frac{2}{3}, c_{w1} = \frac{c_{b1}}{k^2} + (1+c_{b2})/\sigma, c_{w2} = 0.3, c_{w3} = 2, k = 0.41, c_{v1} = 7.1, c_{t1} = 1.0, c_{t2} = 2.0, c_{t3} = 1.1, c_{t4} = 2.0$.

The shear stress $\bar{\tau}_{ik}$ and total heat flux $\bar{q}_k$ in Cartesian coordinates is given by

$$\bar{\tau}_{ik} = \left(\mu + \mu_{IDDES}\right)\left[\left(\frac{\partial\tilde{u}_i}{\partial x_k} + \frac{\partial\tilde{u}_k}{\partial x_i}\right) - \frac{2}{3}\delta_{ik}\frac{\partial\tilde{u}_j}{\partial x_j}\right] \tag{12}$$

$$\bar{q}_k = -\left(\frac{\mu}{Pr} + \frac{\mu_{IDDES}}{Pr_t}\right)\frac{\partial\tilde{T}}{\partial x_k} \tag{13}$$

where μ is from Sutherland's law. For IDDES approach in general, the eddy viscosity is represented by $\mu_{IDDES}(= \bar{\rho}\tilde{\nu}f_{v1})$.

2.2 Improved Delayed Detached Eddy Simulation (IDDES)

The IDDES solver implemented and validated by Yang and Zha [28, 29] is adopted in this study.

The Improved DDES (IDDES) is introduced by extending the DDES with the WMLES capacity. The IDDES has two branches, DDES and WMLES, including a set of empirical functions of subgrid length-scales designed to achieve good performance from these branches themselves and their coupling. By switching the activation of RANS and LES in different flow regions, IDDES significantly expands the scope of application of DDES with well-balanced and powerful numerical approach to complex turbulent flows at high Reynolds numbers.

The three aspects of IDDES are presented below: the DDES branch, the WMLES branch and hybridization of DDES and WMLES.

DDES branch of IDDES

This branch is responsible for the DDES-like functionality of IDDES and should become active only when the inflow conditions do not have any turbulent content (if a simulation has spatial periodicity, the initial conditions rather than the inflow conditions set the characteristics of the simulation), in particular when a grid of "boundary-layer type" precludes the resolution of the dominant eddies. The DDES formulation can be reformulated as

$$l_{DDES} = l_{RANS} - f_d max\{0, l_{RANS} - l_{LES}) \tag{14}$$

where the delaying function, f_d, is defined the same as

$$f_d = 1 - tanh[(8r_d)^3] \tag{15}$$

and the quantity r_d borrowed from the S-A RANS turbulence model

$$r_d = \frac{\nu_t + \nu}{k^2 d_w^2 max[(U_{i,j}U_{i,j})^{0.5}, 10^{-10}]} \tag{16}$$

is a marker of the wall region, which is equal to 1 in a log layer and 0 in a free shear flow.

In Eq. 16, $U_{i,j}$ represents the velocity gradient, and k denotes the Karmann constant. Based on the general DES concept, in order to create a seamless hybrid model, the length-scale IDDES defined by Eq. 14 is substituted into the background RANS model to replace the RANS length-scale, l_{RANS}, which is explicitly or implicitly involved in any such model. For instance, for the S-A model the length-scale is equal to the distance to the wall $l_{RANS} = d_w$. In the original DES97, the length-scale depends only on the local grid. In DDES and IDDES, it also depends on the solution of Eqs. 14 & 16.

As far as the LES length-scale, l_{LES}, in Eq. 14 is concerned, it is defined via the subgrid length-scale as

$$l_{LES} = C_{DES}\Phi\Delta \tag{17}$$

where C_{DES} is the fundamental empirical constant of DES, 0.65. Φ is a low-Reynolds number correction introduced in order to compensate the activation of the low-Reynolds number terms of some background RANS model in LES mode. Both C_{DES} and Φ depend on the background RANS model, and Ψ is equal to 1 if the RANS model does not include any low-Reynolds number terms.

WMLES branch of IDDES

This branch is intended to be active only when the inflow conditions used in the simulation are unsteady and impose some turbulent content with the grid fine enough to resolve boundary-layer dominant eddies. It presents a new seamless hybrid RANS-LES model, which couples RANS and LES approaches via the introduction of the following blended RANS-LES length-scale:

$$l_{WMLES} = f_B(1 + f_e)l_{RANS} + (1 - f_B)l_{LES} \tag{18}$$

The empirical blending-function f_B depends upon d_w/h_{max} and is defined as

$$f_B = min\{2exp(-9\alpha^2), 1.0\}, \alpha = 0.25 - d_w/h_{max} \tag{19}$$

It varies from 0 to 1 and provides rapid switching of the model from RANS mode ($f_B = 1.0$) to LES mode ($f_B = 0$) within the range of wall distance $0.5h_{max} < d_w < h_{max}$

The second empirical function involved in Eq. 18, elevating-function, f_e, is aimed at preventing the excessive reduction of the RANS Reynolds stresses observed in the interaction of the RANS and LES regions in the vicinity of their interface. It is intended to eliminating the log-layer mismatch(LLM) problem.

$$f_e = max\{(f_{e1} - 1), 0\}\Phi f_{e2} \tag{20}$$

where the function f_{e1} is defined as

$$f_{e1}(d_w/h_{max}) = \begin{cases} 2exp(-11.09\alpha^2) & \text{if } \alpha \geq 0 \\ 2exp(-9.0\alpha^2) & \text{if } \alpha < 0 \end{cases} \tag{21}$$

It provides a grid-dependent "elevating" device for the RANS component of the WMLES length-scale.

The function f_{e2} is: $$f_{e2} = 1.0 - max\{f_t, f_l\} \tag{22}$$

Blending DDES and WMLES branches

The DDES length-scale defined by Eq. 14 and that of the WMLES-branch defined by Eq. 18 do not blend directly in a way to ensure an automatic choice of the WMLES or DDES mode by the combined model, depending on the type of the simulation (with or without turbulent content) and the grid used.

However a modified version of equivalent length scale combination, namely,

$$\tilde{l}_{DDES} = \tilde{f}_d l_{RANS} + (1 - \tilde{f}_d)l_{LES} \tag{23}$$

where the blending function $\tilde{f}_d$ is defined by

$$\tilde{f}_d = max\{(1 - f_{dt}), f_B\} \tag{24}$$

with $f_{dt} = 1 - tanh[(8r_{dt})^3]$

With the use of Eq. 23, the required IDDES length-scale combining the DDES and WMLES length scales defined by Eqs. 23 & 18 is straightforward and can be implemented as

$$l_{hyb} = \tilde{f}_d(1 + f_e)l_{RANS} + (1 - \tilde{f}_d)l_{LES} \tag{25}$$

With inflow turbulent content, f_{dt} is close to 1.0, $\tilde{f}_d$ is equal to f_B, so Eq. 25 is reduced to $l_{hyb} = l_{WMLES}$ in Eq. 18. Otherwise, f_e is zero. Equation 25 is interpreted as $l_{hyb} = l_{DDES}$ in Eq. 23.

2.3 Time Marching Scheme

Following the dual time stepping method suggested by Jameson [30], an implicit pseudo-time marching scheme using line Gauss-Seidel line relaxation is employed to solve the governing equations, as the following:

$$\frac{\partial \mathbf{Q}}{\partial t} = \frac{3\mathbf{Q^{n+1}} - 4\mathbf{Q^{n}} + \mathbf{Q^{n-1}}}{2\Delta t} \tag{26}$$

where $n-1$, n and $n+1$ are three sequential time levels, which have a time interval of Δt. The first-order Euler scheme is used to discretize the pseudo-temporal term. The semi-discretized equations of the governing equations are given as the following:

$$\begin{aligned} &\left[\left(\tfrac{1}{\Delta\widehat{\tau}} + \tfrac{1.5}{\Delta t}\right) I - \left(\tfrac{\partial R}{\partial \mathbf{Q}}\right)^{n+1,m}\right] \delta\mathbf{Q^{n+1,m+1}} \\ &\quad = R^{n+1,m} - \tfrac{3\mathbf{Q^{n+1,m}} - 4\mathbf{Q^{n}} + \mathbf{Q^{n-1}}}{2\Delta t} \end{aligned} \tag{27}$$

where the $\Delta\widehat{\tau}$ is the pseudo time step, and R stands for the net flux determined by the spatial high order numerical scheme, m is the iteration index for the pseudo time. A non-dimensional physical time-step of 0.0003 is used for the present study. Up to 40 psuedo-time steps are used within each physical time step at CFL = 5.0. Pseudo-time convergence is truncated if $||L_2||$ converges five orders of magnitude.

2.4 Navier-Stokes Solver

The high order accuracy CFD code Flow-Acoustics-Structure Interaction Package (FASIP) is used to conduct the numerical simulation. The 3D Navier-Stokes equations given in Section 2.1 are solved by a 5th order WENO scheme for the inviscid flux [31, 32, 33] and a 4th order central differencing scheme for the viscous terms [32]. The low diffusion E-CUSP scheme suggested by Zha et al [34] is utilized with the WENO scheme to evaluate the inviscid fluxes. This E-CUSP scheme is based on the Zha-Bilgen flux-vector-splitting scheme [35], and is used as the approximate Riemann solver. An implicit time marching method using Gauss-Seidel line relaxation is used to achieve a fast convergence rate [36]. Parallel computing is implemented to save simulation time [37]. The FASIP code has been intensively validated for CFJ flow control simulations [7, 10, 11, 12, 26, 38, 39, 40, 41].

2.5 CoFlow Jet Parameters

2.5.1 Jet Momentum Coefficient

The jet momentum coefficient, C_μ, is a parameter used to quantify the injection jet "strength". It is defined as

$$C_\mu = \frac{\dot{m} V_j}{\frac{1}{2}\rho_\infty {V_\infty}^2 S} \tag{28}$$

where $\dot{m}$ is the injection jet mass flow, V_j the injection jet velocity, ρ_∞ and V_∞ are the freestream density and velocity, and S is the reference area.

2.5.2 C_μ Iteration

In previous CFJ studies using FASIP, the following CFJ C_μ implementation is used. To achieve zero net mass flux with the CFJ flow control, the mass flow exiting the injection slot must be equal to the mass flow entering the suction slot, i.e. $\dot{m}_{inj} = \dot{m}_{suc}$. The prescribed jet momentum coefficient C_μ is achieved by iteratively adjusting the injection cavity total pressure. Injection total temperature is assumed to be equal to the freestream total temperature to simplify the boundary condition implementation. This assumption has been shown to be valid for many previous CFJ studies because of the very low total pressure ratio required to drive the CFJ fluidic actuator. The injection and suction mass flow rates are matched by then adjusting the suction cavity static pressure. The iterative process is conducted throughout the simulation until the specified momentum coefficient is reached and the injection and suction mass flow match within an acceptable tolerance, typically 1%.

In this study, the CFJ C_μ implementation is modified to vary the CFJ injection boundary total temperature. The prescribed jet momentum coefficient C_μ is achieved by adjusting the injection cavity total pressure AND total temperature. After the total pressure is iterated, total temperature is calculated to match using the isentropic flow relation Eq. 29. The injection and suction mass flow rates are matched by then adjusting the suction cavity static pressure. The iterative process is conducted throughout the simulation until the specified momentum coefficient is reached and the injection and suction mass flow match within an acceptable tolerance, which is 0.5% for the present study.

$$T_{01}/T_{02} = \frac{(P_{01}/P_{02})^{\frac{\gamma-1}{\gamma}} - 1}{\eta} + 1 \tag{29}$$

2.5.3 Pumping Power

The CFJ is implemented via a pumping system inside the wing that draws air from the suction slot and blows it out of the injection slot. As a zero net mass flux flow control mechanism with a closed flow path, the CFJ power required can be defined using the thermodynamic relationship based on the mass flow rate and total enthalpy difference as

$$P = \dot{m}(H_{t1} - H_{t2}) \tag{30}$$

where H_{t1} and H_{t2} are the total enthalpy in the injection cavity and suction cavity respectively, P is the power required by the pump and $\dot{m}$ the jet mass flow rate. Introducing the pumping efficiency η and total pressure ratio of the pump $\Gamma = \frac{P_{t1}}{P_{t2}}$, the power required can be expressed as :

$$P = \frac{\dot{m} C_p T_{t2}}{\eta}(\Gamma^{\frac{\gamma-1}{\gamma}} - 1) \tag{31}$$

This power required is normalized as the power coefficient, given as

$$P_c = \frac{P}{\frac{1}{2}\rho_\infty V_\infty^3 S} \tag{32}$$

In this research, the CFJ pumping efficiency is set to 70% to reflect estimated compressor efficiency from a recent paper from Barrios et al. [14]. Fig. 2 shows an example compressor map of the latest CFJ micro-compressor design. Eq. 31 indicates that the power required by the CFJ is determined linearly by the mass flow rate and exponentially by the total pressure ratio. Large injection slots reduce the power required because the total pressure loss in the injection duct is substantially reduced. It follows that the most efficient way to implement the CFJ is to employ a large mass flow rate and low total pressure ratio.

2.5.4 Corrected Aerodynamic Efficiency

An airfoil's aerodynamic efficiency is conventionally defined as $\frac{L}{D}$. Since CFJ active flow control consumes energy, the corrected aerodynamic efficiency is modified to take into account the energy consumption of the pump. The formulation of the corrected aerodynamic efficiency for CFJ airfoils is

$$\left(\frac{C_L}{C_D}\right)_c = \frac{L}{D + \frac{P}{V_\infty}} = \frac{C_L}{C_D + P_c} \tag{33}$$

where V_∞ is the freestream velocity, P is the CFJ pumping power, and C_L and C_D are the lift and drag coefficients. This formulation essentially converts the power consumed by the CFJ into drag of the CFJ system.

2.5.5 Lift and Drag Calculation

The momentum and pressure at the injection and suction slots produce a reactionary force not included in the surface integral used to calculate lift and drag on the airfoil surface. Using control volume analysis, the reactionary force can be calculated using the flow parameters at the injection and suction slot openings.

Zha et al. [10] give the following formulations to calculate the lift and drag due to the jet reactionary force for a CFD simulation. By considering the effects of injection and suction jets on the CFJ airfoil, the expressions for these reactionary forces are

$$F_{x_{cfj}} = (\dot{m}_j V_{j1} + p_{j1} A_{j1}) * \cos(\theta_1 - \alpha) - (\dot{m}_j V_{j2} + p_{j2} A_{j2}) * \cos(\theta_2 + \alpha) \tag{34}$$

$$F_{y_{cfj}} = (\dot{m}_{j1} V_{j1} + p_{j1} A_{j1}) * \sin(\theta_1 - \alpha) + (\dot{m}_{j2} V_{j2} + p_{j2} A_{j2}) * \sin(\theta_2 + \alpha) \tag{35}$$

where the subscripts 1 and 2 stand for the injection and suction respectively, and θ_1 and θ_2 are the angles between the injection and suction slot surfaces and a line normal to the airfoil chord. α is the angle of attack.

The total lift and drag on the airfoil can then be expressed as:

$$D = R'_x - F_{x_{cfj}} \tag{36}$$

$$L = R'_y - F_{y_{cfj}} \tag{37}$$

where R'_x and R'_y are the surface integral of pressure and shear stress in x (drag) and y (lift) direction excluding the internal ducts of injection and suction. The total lift and drag are calculated using Eqs. 36–37.

2.6 Computational Mesh Geometry and Flow Conditions

The geometries of the CFJ and baseline airfoils are adopted our previous 2D and 3D studies [3, 17]. Both meshes have significantly refined mesh spacing in areas around the airfoil and wake region for better resolution of turbulent eddies via LES. The baseline airfoil is the NACA6421 airfoil, simulated at $\alpha = 14°$, the $C_{L_{max}}$ condition found in the prior 3D study [3]. The CFJ airfoil is simulated at $\alpha = 65°$.

The 3D multiblock structured meshes for the baseline and CFJ airfoils are constructed using an O-mesh topology in order to achieve high mesh quality near airfoil wall surfaces. For the CFJ airfoil mesh, 2001 grid points are distributed circumferentially around the airfoil, with 601 points on the lower surface and 1401 points on the upper surface, 301 points distributed radially from the airfoil, and 51 points in the spanwise direction. For the CFJ slots and suction surface translation region, there are 61 points distributed across the jet. The mesh is partitioned for parallel computation. Table 1 details the mesh parameters for each case.

Table 1: Mesh parameters

Case	$N_\xi \times N_\eta \times N_\zeta$	Total Cells	Blocks	$\Delta x_{1_{min}}$	$\Delta x_{1_{max}}$	Δy_1	Δz
Baseline	$1600 \times 175 \times 50$	13,200,000	280	2.0×10^{-5}	1.37×10^{-2}	1.0×10^{-6}	0.002
CFJ	$2000 \times 300 \times 50^*$	14,600,000	308	1.0×10^{-4}	1.37×10^{-2}	1.0×10^{-6}	0.002

* The grid points around the airfoil exclude the CFJ injection and suction blocks.

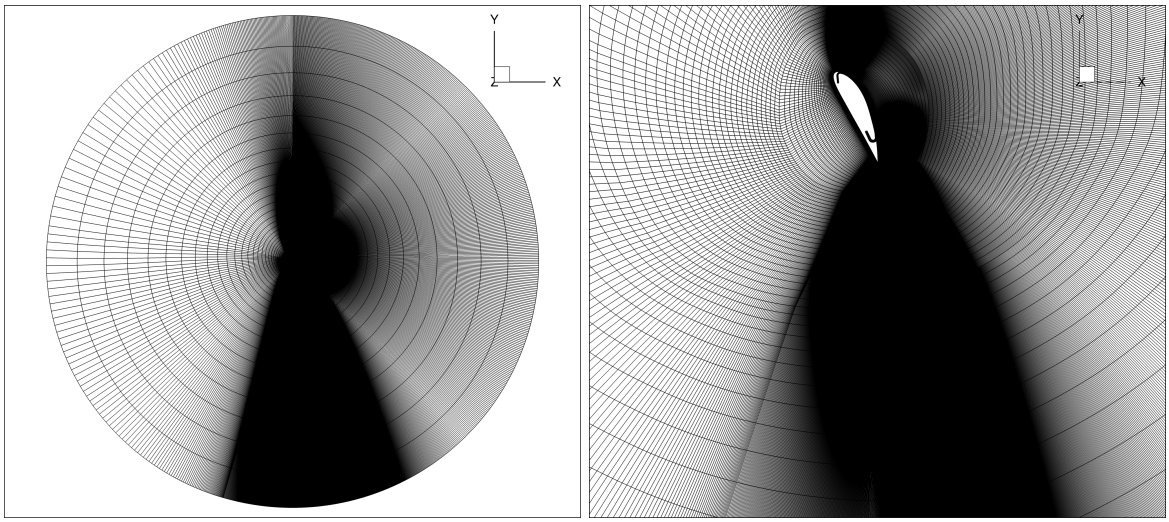

Figure 3: Computational mesh for CFJ airfoil far field with additional cells to resolve the wake.

The far-field boundary is located 200 chords away from the airfoil. The simulated CFJ wing span is 10% the chord length, with periodic boundary conditions applied on the spanwise domain faces. To resolve the turbulent boundary layer, the first grid point is placed at or below $y^+ \approx 1$. Local y^+ is confirmed less than 1.0 in post-processing. A cross section of the mesh showing the far field and density of cells around the airfoil is given in Fig. 3, which shows that the mesh is refined downstream of the airfoil to resolve the turbulent wake. The surface mesh for the CFJ airfoil is shown in Fig. 4. There is a greater cell density near the CFJ injection and suction slot openings, and along the tail, where the flow has greater turbulence.

Improved Delayed Detached Eddy Simulation is used to model the 3D unsteady, turbulent flows of both the 3D baseline NACA6421 airfoil and CFJ6421 airfoil. Identical numerical methods are used in both cases. A normalized physical time step of 3.0×10^{-4} is used with a CFL number of 10.0 applied for the pseudo time iteration. Up to 40

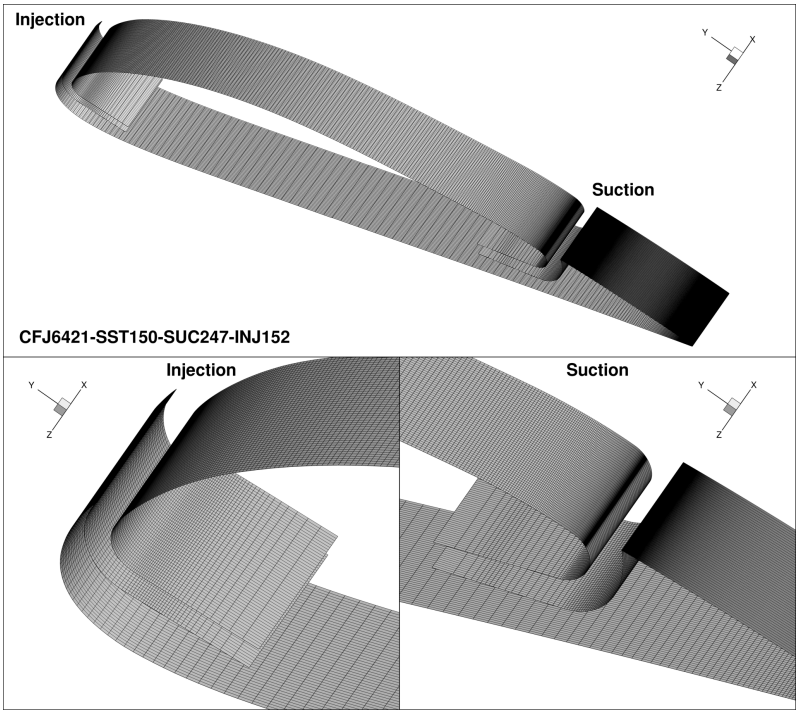

Figure 4: CFJ airfoil surface mesh.

pseudo-time steps are used; the iteration progresses to the next step if the maximum L2-norm residual is reduced 6 orders of magnitude within a physical time step. The interface flux of the inviscid conservative variables is evaluated using a 5^{th} order WENO scheme with the Zha-Bilgen low-diffusion E-CUSP scheme to reduce numerical dissipation. The viscous terms are solved using 4^{th} order central differencing, ensuring that the stencil width falls within the WENO stencil for numerical stability. A freestream Mach number of 0.063 and freestream Reynolds number of 5.62×10^5 are used. A $C_\mu = 2.5$ is used to sustain attached flow and create a super-lift coefficient. Each case was run for a minimum of 100 characteristic time, $\bar{t}$. All results are taken once the trailing-time-averaged aerodynamic forces no longer vary. The "Hot Jet" case was initialized from the final flow field of the "Cold Jet" case and allowed to run until it showed stable trailing-time-averaged results.

2.7 Boundary Conditions

Freestream conditions including total pressure, total temperature, and flow angle are specified for the upstream portion of the far field boundary. For far field downstream boundary, the static pressure is specified as freestream value to match the intended freestream Mach number. The periodic boundary condition is applied in the spanwise direction. The wall treatment suggested in [31] to achieve flux conservation by shifting half interval of the mesh on the wall is employed. This method has third-order accuracy on the wall. If the wall surface normal direction is in η-direction, the no slip condition is enforced on the surface by computing the wall inviscid flux $F_{1/2}$ in the following manner:

$$\mathbf{F_w} = \begin{pmatrix} \rho V \\ \rho u V + p\eta_x \\ \rho v V + p\eta_y \\ \rho w V + p\eta_z \\ (\rho e + p)V \end{pmatrix}_w = \begin{pmatrix} 0 \\ p\eta_x \\ p\eta_y \\ p\eta_z \\ 0 \end{pmatrix}_w \tag{38}$$

3 Comparison of Hot Jet and Cold Jet Flow Fields

3.1 Flow Fields

Compared to the Cold Jet case, the jet flow of the Hot case is more energetic, more turbulent, and more unsteady. Figure 5 shows Mach contours of a mid-plane slice of the Cold case. The same slice for the Hot case, shown in Fig. 6, shows significantly more turbulent eddies outside of the wall jet. While there appears to be a clear delineation between the wall jet flow and the external flow in the Cold case, that distinction is much more diffused for the Hot case. For the Hot case, large scale shear layer instability begins close to the maximum thickness location, while the Cold case shows shear layer instability farther downstream, slightly before the suction slot. The Cold case exhibits periodic shedding of the Kelvin-Helmholtz Instability, which can be seen in this Mach contour field by the alternating high speed / low speed zones along the tail surface, and by the vortex tubes visible above the suction slot in Figure 11 (Bottom Left). The Hot case does not appear to show an organized vortex shedding process, and the highly turbulent region extends much father from the airfoil surface and into the wake (Figs. 6 & 11).

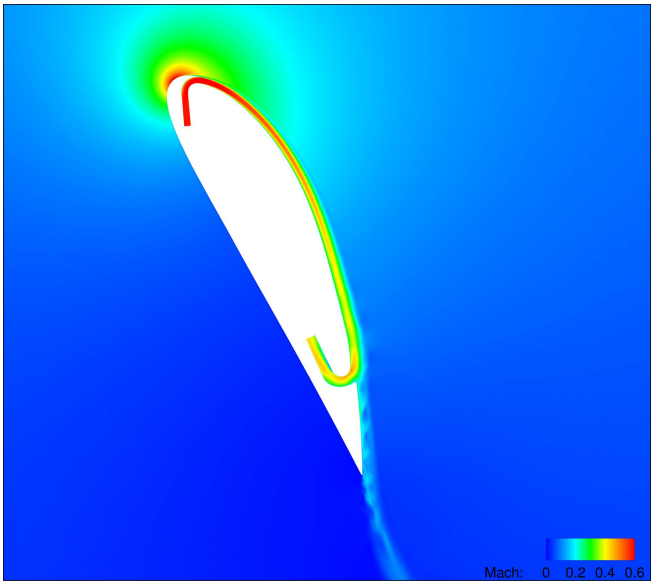

Figure 5: Inst. midplane "Cold" CFJ Mach contours

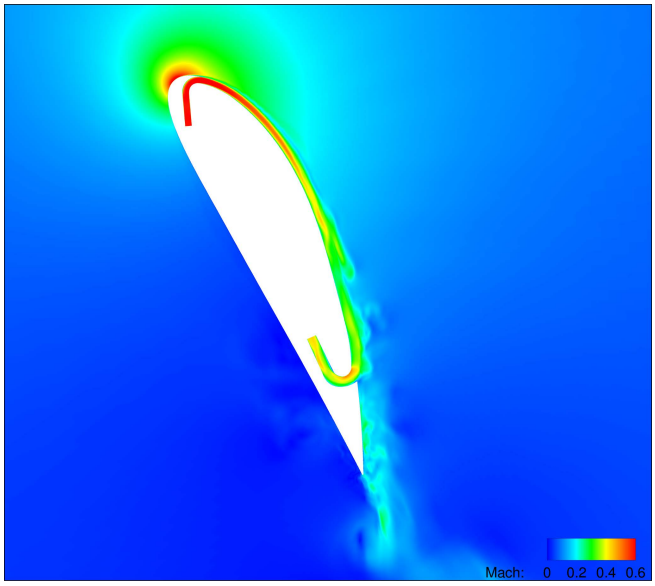

Figure 6: Inst. midplane "Hot" CFJ Mach contours

While the Hot Jet flow is significantly more turbulent than the Cold Jet flow, Figures 7–8 show that the streamlines of the time-averaged flow fields remain similar. Because the circulation of the airfoil is very large, the leading edge stagnation point moves from the airfoil's leading edge to a position on the pressure surface very close to the trailing edge. The flow field structure of the 3D CFJ airfoil simulations are largely similar to that of the 2D airfoil simulation for the same conditions [17]. The 2D study showed that additional detached stagnation points would form around a circulating region below the airfoil for $C_L \geq 12.38$ [17]. Consistent with the 2D study, the stagnation points for these 3D simulations remain on to the surface of the airfoil. The time-averaged flow field streamlines form a sharp cusp below the trailing edge of the airfoil, but a detached stagnation point with a distinct circulating region requires greater circulation. The circulation the CFJ can add to the flow field is limited in part by the jet injection Mach number. The maximum Mach number around the inner turn of the CFJ injection duct reaches about 0.85 for both cases. A higher C_μ would lead to choked flow in the injection duct, preventing the CFJ airfoil from adding sufficient circulation to the external flow field which would lead to the formation of the detached stagnation point.

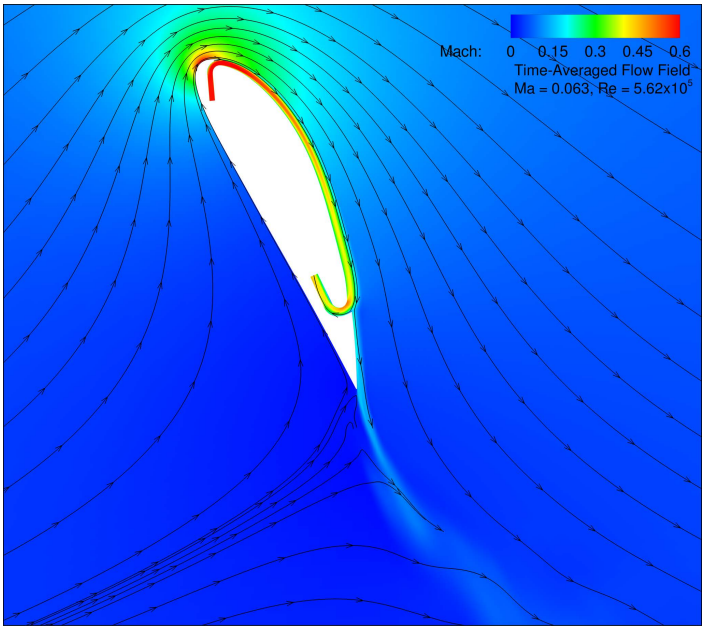

Figure 7: "Cold" CFJ time-averaged Mach contours with streamlines

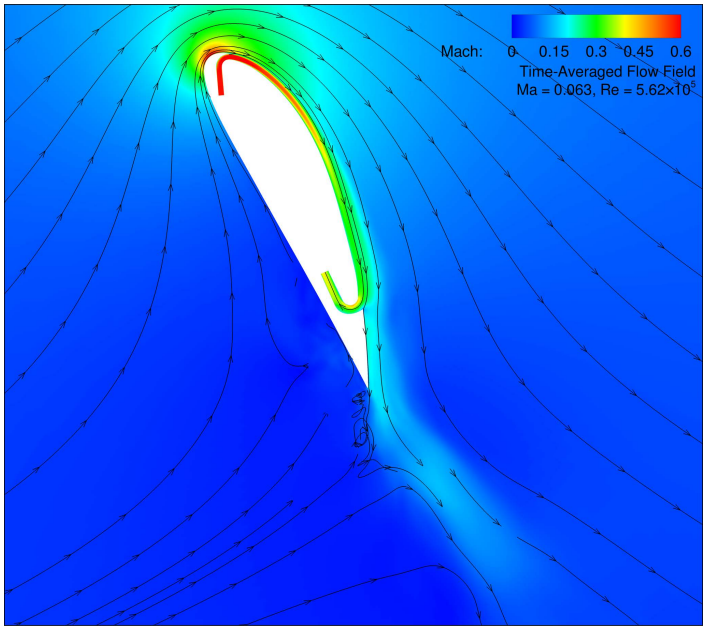

Figure 8: "Hot" CFJ time-averaged Mach contours with streamlines

3.2 Vortical Structures

Figures 9–10 are Q-criterion iso-surfaces, used to qualitatively visualize the vortical structures around the CFJ airfoil. The iso-surfaces are colored by the total vorticity, ω_t, using different color scales, because the Hot Jet case shows ω_t values at least an order of magnitude higher than the Cold Jet case. The vortical structures of the Cold Jet CFJ show that the leading edge and injection jet flows are very stable, until the shear layer instability forms just downstream of the airfoil's point of maximum thickness. The Kelvin-Helmholtz Instability is shown by the

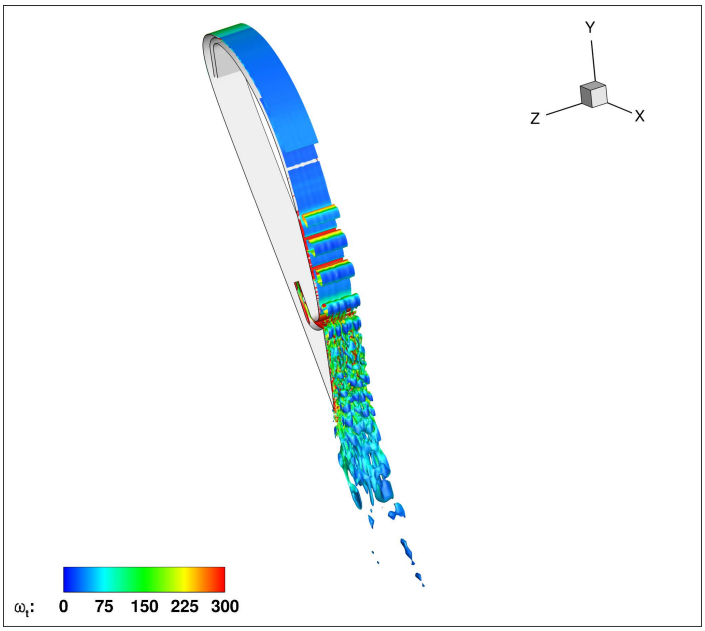

Figure 9: Cold Jet Q iso-surfaces, full airfoil

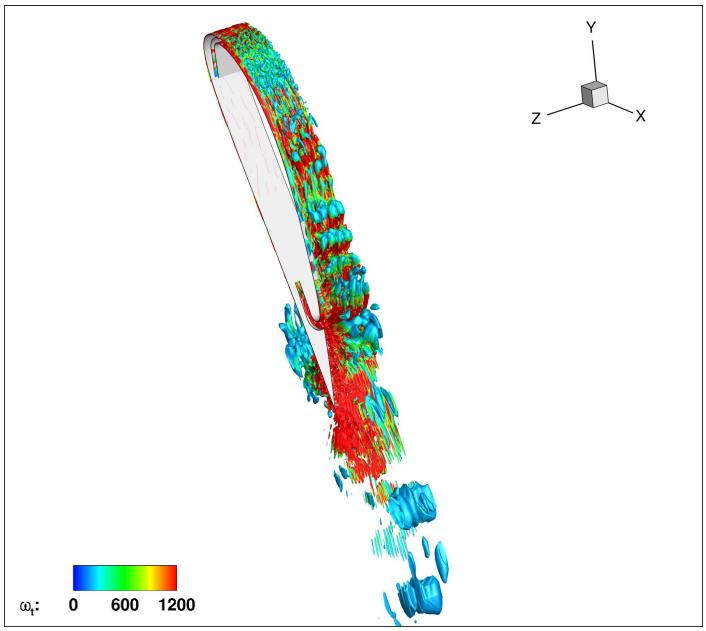

Figure 10: Hot Jet Q iso-surfaces, full airfoil

periodic spanwise vortex tubes approaching the suction duct. Once the flow reaches the sharp lip of the suction duct, the spanwise vortex structures break down into more complex structures, gaining significant streamwise and normal vorticity components [3]. The vortical structures are far more significant in the Hot Jet case, which shows strong vortical flow around the entire surface of the airfoil. Unlike the Cold Jet case, for which the flow is primarily spanwise-vortex-dominant on the suction surface, the Hot Jet case shows vortices with sizeable ω_s and ω_n components. The vortical flow extends farther from the airfoil's surface, and into the airfoil wake. The strong turbulent fluctuations near the airfoil's trailing edge influence the incoming flow at the "leading edge" of the airfoil (see streamlines of Figs. 7–8). This unsteady flow can be seen as a thin layer travelling along the Hot Jet airfoil's pressure surface, until it reaches the injection slot.

Figure 11 again shows the Q-criterion iso-surfaces colored by total vorticity, focusing on the regions near injection suction slots. The Cold Jet CFJ shear layer appears as a thin sheet in the Q-criterion, separating regions of positive and negative spanwise vorticity. Clearly, the large vortex structures of the Hot Jet case originate upstream of the injection slot, propagating from the trailing edge instability. The vortical structures are greatly enhanced in the mixing layer immediately downstream of the injection slot's outer lip. The bottom left plot of Fig. 11 more clearly shows the KHI of of the Cold Jet CFJ. While there is evidence of the shear layer "rolling up" in the Hot Jet CFJ, it is much less organized than the Cold Jet do to the interaction with the flow's out-of-plane vorticity components.

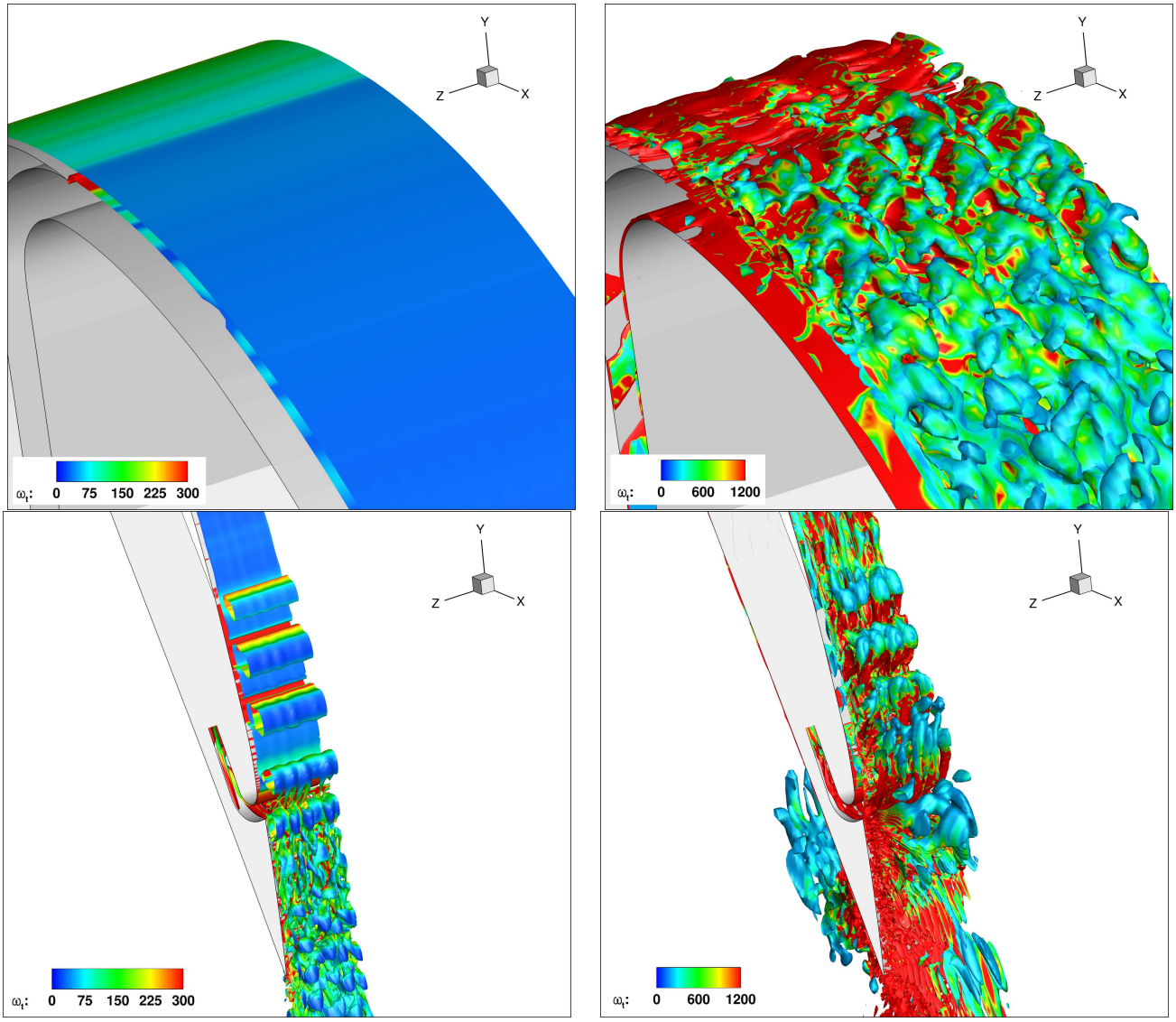

Figure 11: Q-criterion iso-surfaces.

Figures 12–13 show the iso-surfaces of the streamwise vorticity at $\omega_s = \pm 25$. The Cold case has very little ω_s upstream of the suction inlet, while the Hot case has streamwise vorticity along the entire surface and into the wake. The stronger vorticity contributes to increased mixing between the flow local to the CFJ and the main flow.

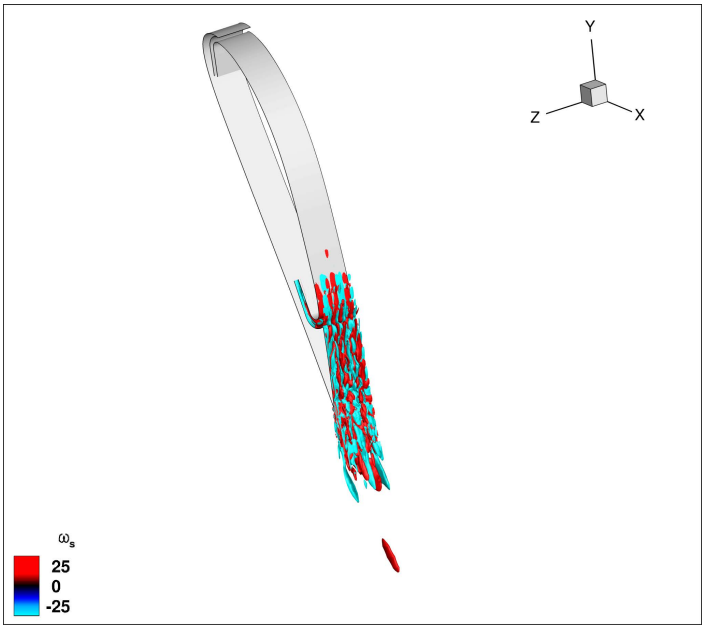

Figure 12: Cold ω_s iso-surfaces, full airfoil

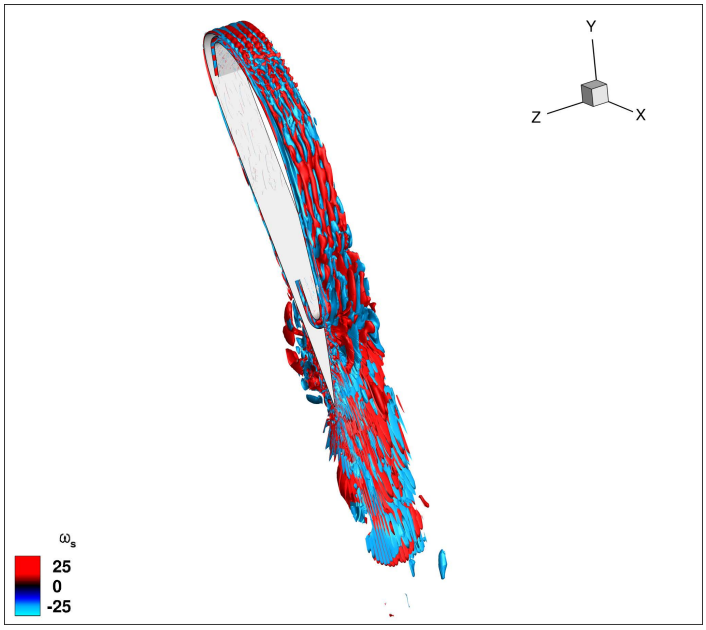

Figure 13: Hot ω_s iso-surfaces, full airfoil

Figure 14 shows the iso-surfaces of the streamwise vorticity, focused on the injection slot region. The iso-surfaces for the Cold Jet case are drawn at a value 100 times smaller than the Hot Jet case, because the ω_s component is so small in the injection region, it would not be visible at a higher scale. The steady injection flow of the Cold Jet case is shown in the left plots, and the turbulent injection flow of the Hot Jet case is shown in the right plots.

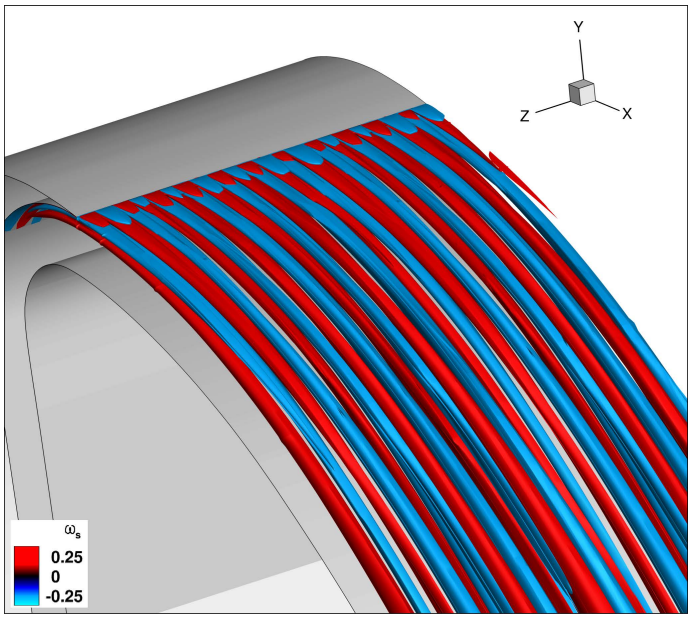

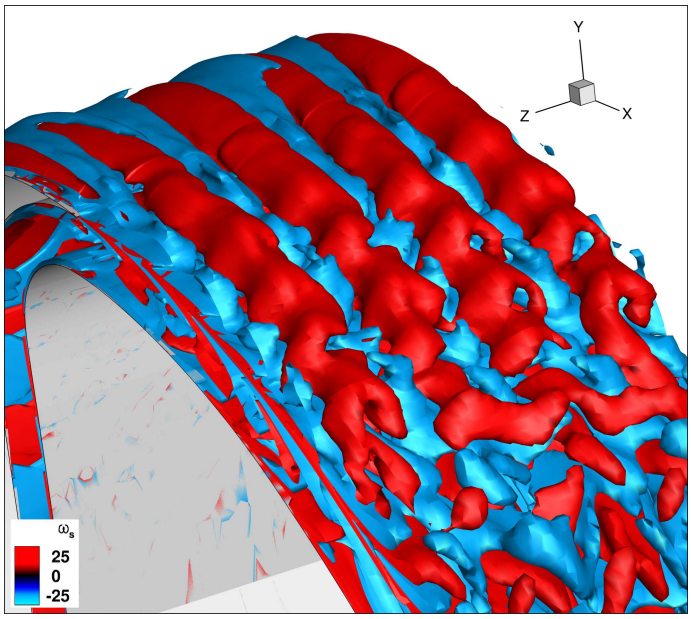

Figure 14: ω_s iso-surfaces.
Cold Jet injection (Left), Hot Jet injection (Right)

3.2.1 Vorticity Generation in CFJ Injection Duct

The CFJ injection jet creates the high-speed turbulent wall jet on the suction surface of the airfoil. It is this turbulent wall jet which transfers momentum and energy to the main flow, enabling the super-lift capability of the airfoil, and drastically increasing the stall margin. Turbulent jets are better at maintaining attached flow, and enable greater rates of momentum and energy transfer due to the turbulence diffusion.

The CFJ injection jet enters the main flow field with two counter-rotating layers of very strong spanwise vorticity. The clockwise layer forms on the inner duct wall, while the counterclockwise layer forms on the outer duct wall. These layers are formed by the wall shear layer. A third clockwise layer is formed due to shear along the airfoil leading edge, and a fourth counterclockwise layer is induced in the flow as the conjugate to the third layer. Figures 15–16 compare the spanwise vorticity fields of the CFJ injection region. Blue regions are clockwise, red regions are counter-clockwise. Both plots show the four vortex layers, although the fourth layer is very thin for the Cold case, Fig. 15. The vortex layers of the Hot Jet case shown in Fig. 16 are not cleanly divided like they are in the Cold Jet case. This is due to the significant vorticity and turbulence generated in the Hot Jet case's injection jet flow which is not present in the Cold Jet case. This motivates the question: Why does the CFJ injection flow have drastically more out-of-plane vorticity when the flow's total enthalpy is higher?

Figure 15: Spanwise Vorticity layers at CFJ Injection mid-plane, Cold Case

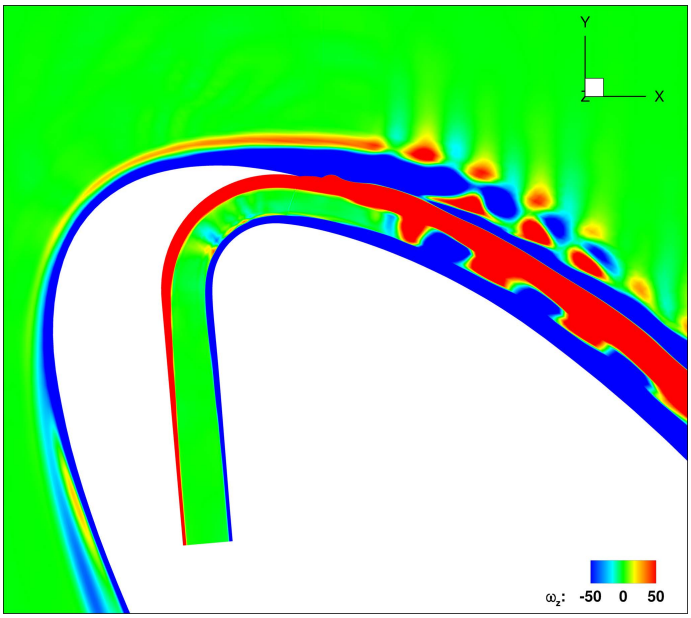

Figure 16: Spanwise Vorticity layers at CFJ Injection mid-plane, Hot Case

The out-of-z-plane vorticity creation of the Hot Jet case is attributed to the difference in thermodynamic potential from the higher total enthalpy of the flow. Crocco's Theorem conveniently simplifies the vorticity equation to relate the thermodynamic and kinematic properties of a fluid element travelling along a streamline. The x- and y- vorticity is generated away from the duct walls, and is assumed to be created by inviscid forces. It is implied that streamlines originating from a common reservoir (such as the flow originating from the CFJ inlet boundary condition) have a uniform total enthalpy, H_t. Such a flow is termed *homoenergetic*. Because Crocco's equation is derived with the homoenergetic assumption, we can use only this equation to evaluate the flow within the injection duct. It may not be appropriate to use this equation to evaluate the flow outside of the CFJ's free shear layer, where streamlines can come from either the CFJ or from the freestream flow.

The equations of motion of a fluid can be expressed in a form relating the vorticity to the kinematic and thermodynamic properties of the flow. Substituting the Gibbs equation into the conservation of streamwise momentum equation,

$$-\frac{\partial \mathbf{u}}{\partial t} + (\mathbf{u} \times \omega) = \nabla h - T\nabla s + \frac{1}{2}\nabla(u^2)) + F_B + F_v \tag{39}$$

If we assume that the relationship between the flow vorticity and kinematics is derived from inviscid properties, and if we ignore body forces, this equation is further simplified to

$$-\frac{\partial \mathbf{u}}{\partial t} + (\mathbf{u} \times \omega) = \nabla(h + \frac{1}{2}u^2) - T\nabla s = \nabla h_t - T\nabla s \tag{40}$$

Finally, if we assume steady flow, we arrive at Crocco's Theorem, which equates the Lamb vector to the gradient of total enthalpy minus the gradient of the entropy. The Lamb vector, $(u \times \omega \equiv 2\dot{\theta} \times V)$, is not itself vorticity, but represents the centripetal acceleration of a fluid element which is rotating with angular velocity $\dot{\theta}$. Crocco's theorem is a momentum balance equation and thus expresses the equilibrium of all forces acting on the fluid element (inertial and external forces) [42].

$$\mathbf{u} \times \omega = \nabla h_t - T\nabla s \tag{41}$$

For incompressible flows with uniform density away from walls of energy sources or sinks, stagnation pressure loss directly corresponds to entropy generation, and thus Crocco's theorem can be written in terms of stagnation pressure.

$$\mathbf{u} \times \omega = \frac{\nabla p_t}{\rho} \tag{42}$$

Therefore if the stagnation pressure is constant, either the flow is irrotational or the vorticity is parallel to the velocity vector. For compressible flows, the fluid viscous and body forces play the same role as for incompressible flows. Eq. 41 can be rederived from the momentum and Gibbs equations into the form

$$\frac{D}{Dt}(\frac{\omega}{\rho}) = (\frac{\omega}{\rho} \cdot \nabla)\mathbf{u} + \frac{1}{\rho}\nabla T \times \nabla s \tag{43}$$

The quantity ω/ρ for a compressible flow behaves in the same manner as ω alone for an incompressible flow. For baroclinic flows, where the density is a function of both temperature and pressure, the misalignment of the pressure and density fields produces a "baroclinic torque". Vorticity is generated at an angle orthogonal to the intersection of the surfaces of constant pressure and density. In a barotropic (constant temperature) fluid, these surfaces are parallel. The baroclinity is proportional to $\nabla p \times \nabla \rho$.

In a boundary layer subjected to a streamwise pressure gradient, the temperature increases approaching the wall and the density decreases approaching the wall. The density gradient $\nabla\rho$ has streamwise and normal components, while the pressure gradient ∇p is constant normal to the wall, and only has a streamwise component. Thus the density and pressure gradients are not aligned, and the term $\nabla p \times \nabla\rho$ produces a nonzero vorticity. For boundary layer flow in an adverse streamwise pressure gradient, the orientation of $\nabla\rho$ and ∇p is illustrated in Fig. 17.

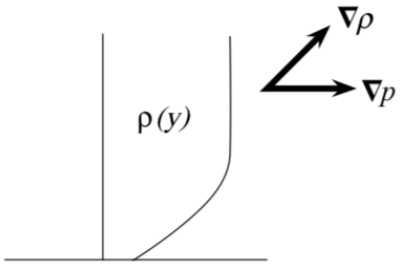

Figure 17: Density and pressure gradients in a boundary layer with an adverse pressure gradient [43].

Crocco's equation indicates that the angular acceleration of a fluid element is caused by the gradients of total enthalpy and entropy. Figure 18 compares the magnitude of the total enthalpy gradient between the Hot and Cold cases on a mid-plane slice of the flow field. While not visible in this slice, this gradient varies significantly in the spanwise direction as well. It is very clear from this comparison that the total enthalpy gradient of the injection jet flow is far more disorganized that that of the Cold Jet case. The Cold case only shows non-zero total enthalpy gradients in the viscous boundary layers along the walls of the injection duct and leading edge. The Hot case shows bands of mild total enthalpy gradient due to the "pulsing" injection flow, which are significantly amplified in the turning of the injection duct.

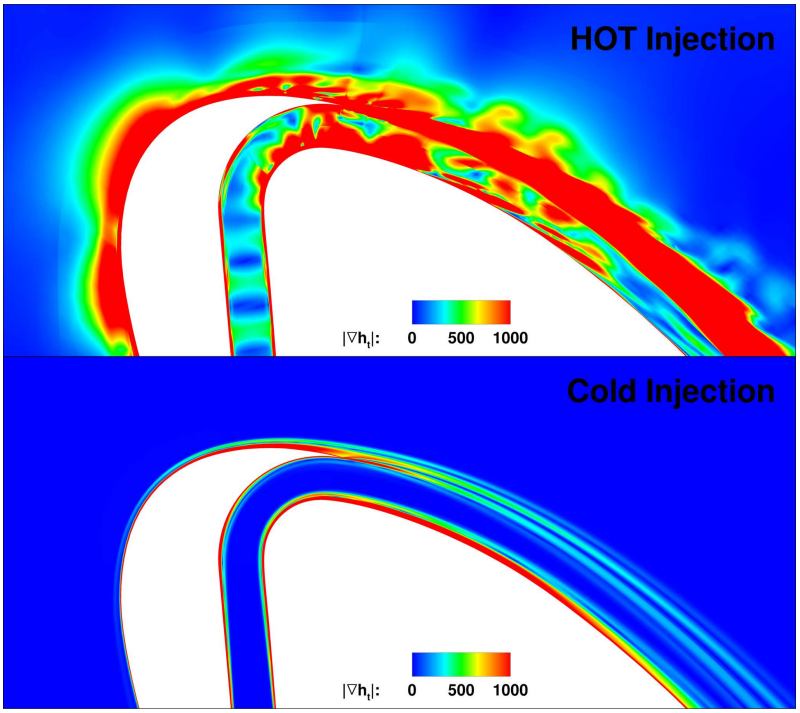

Figure 18: Total Enthalpy Gradient mid-plane comparison

Figure 19 compares the entropy generation between the Hot and Cold cases. The expression $(S - S_\infty)/R$ represents the difference in local entropy and far field entropy, normalized by the Boltzmann constant, R. This figure shows regions of entropy production. The Cold case shows very thin, very mild entropy production in the wall shear layers, and in the wake of the injection duct lip. The Hot case on the other hand shows entropy generation throughout the volume of the jet flow, and much more significant entropy along the wall shear layers. Figure 20 compares the $T\nabla S$ term from Crocco's equation between the Hot and Cold cases. For both cases, the entropy gradient is only significant in the wall shear layer. The Hot case has a somewhat higher enthalpy gradient magnitude, especially in the shear mixing layer in the wake of the injection duct lip.

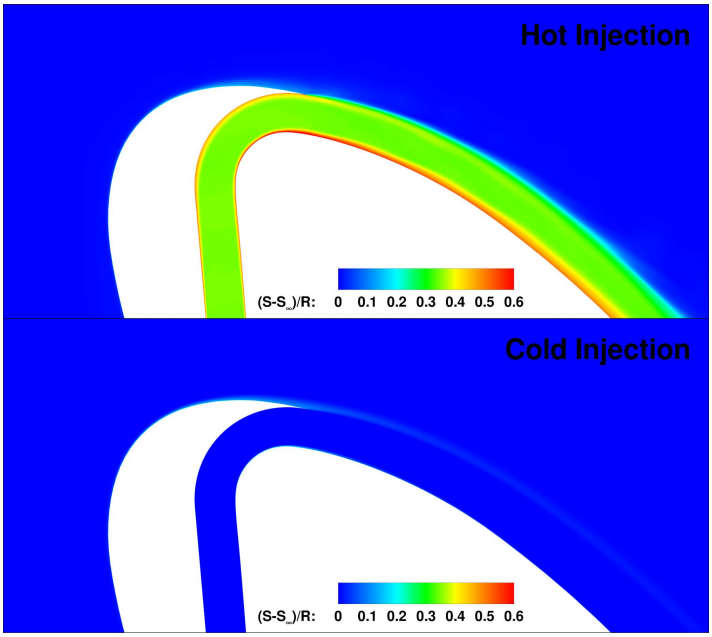

Figure 19: Entropy mid-plane comparison

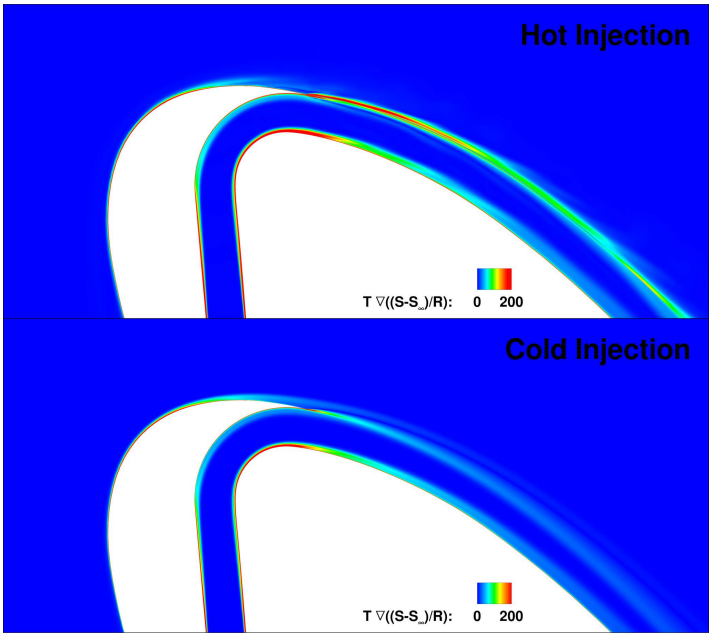

Figure 20: Entropy Gradient mid-plane comparison

Thus, comparing Figures 18 and 20, we make two distinctions. The difference between the ∇H_t and $T\nabla S$ fields is clearly significant, and must cause an angular acceleration out of the z-plane, creating the complex vortical flow in the injection duct. Second, the magnitude of the first term of Crocco's equation, ∇H_t, is far greater than the magnitude of the second term, $T\nabla S$. Thus, the generation of the ω_s and ω_n vorticity components is attributed almost entirely to the gradient of the total enthalpy. This out-of-z-plane gradient is not present in the Cold Jet case, which only observes ω_z in any meaningful magnitude.

3.3 Injection Jet Properties

The injection flow field Mach contours shown in Fig. 21 for the Cold Jet case appear significantly more organized than the Mach contours shown in Fig. 22 for the Hot Jet case. While the former has a very stable flow field around the injection region, the injection flow varies in time for the Hot case. A "pulsing" is observed in the injection flow. This time-variant nature implies misaligned density, pressure, and temperature fields, which creates significantly more turbulence in the injection jet (explained in section 3.2.1). The increased turbulence propagates downstream, where it leads to stronger mixing in the shear layer between the wall jet and the external flow, enabling greater transfer of energy and momentum. The maximum Mach number around the inner turn of the CFJ injection duct reaches about 0.85 for both cases. A higher C_μ would lead to choked flow in the injection duct.

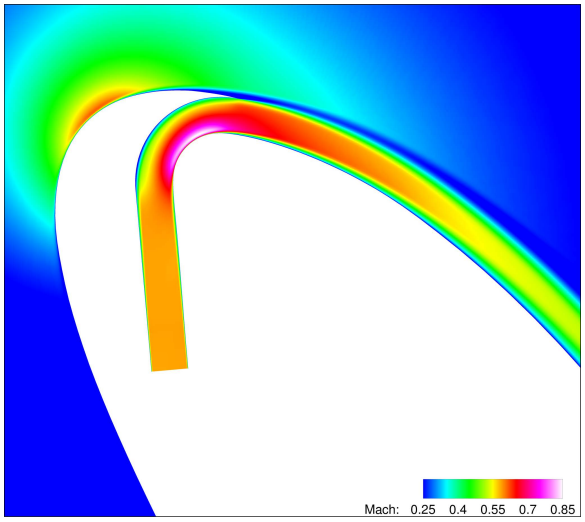

Figure 21: "Cold" CFJ Mach contours, injection

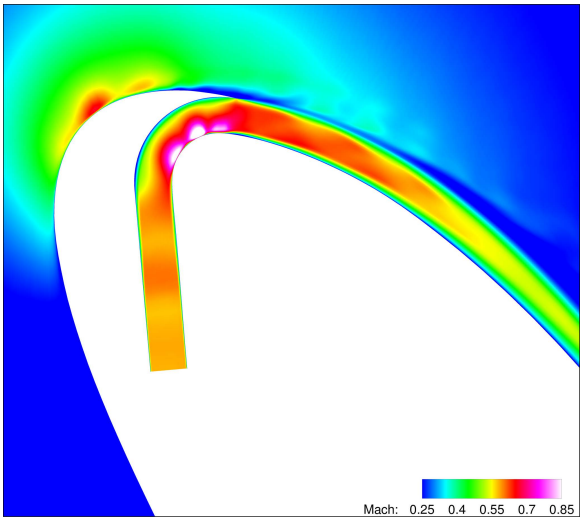

Figure 22: "Hot" CFJ Mach contours, injection

Figure 23 compares the total temperature fields of the two cases. Total temperature is directly analogous to total enthalpy, as $H_t = C_p T_t$. Figure 24 shows the span-averaged distribution of total enthalpy across the injection jet. The vertical axis, D/H, is the distance from the inner wall normalized by the injection slot height. The total enthalpy of the injection jet flow in the Cold case is about the same as the external flow ($D/H > 1$), while the Hot case's jet has a much greater total enthalpy content.

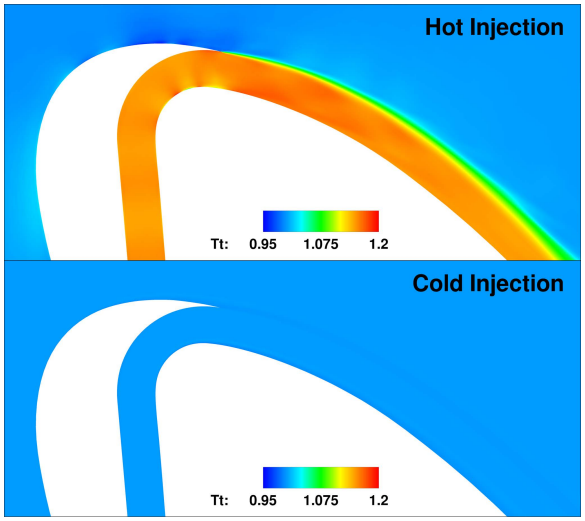

Figure 23: Total Temperature field comparison

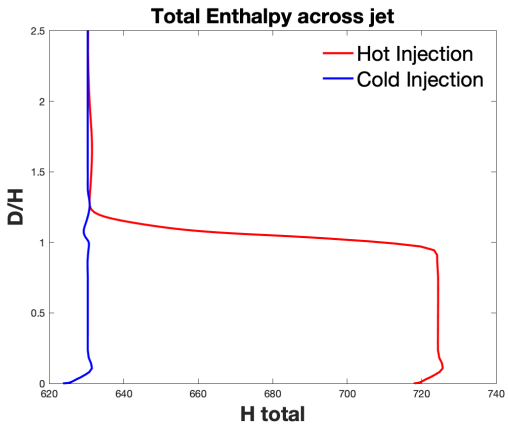

Figure 24: Total Enthalpy distribution comparison

Figure 25 compares the total pressure fields of the two cases. Unlike the total temperature / total enthalpy, the total pressure is about the same between the two cases, as a result of the C_μ iteration process. Figure 26 shows the span-averaged distribution of total pressure across the injection jet. The distributions are nearly identical, with the exception that the Hot case has a shallower total pressure gradient outside of duct, likely due to increased mixing compared to the Cold case.

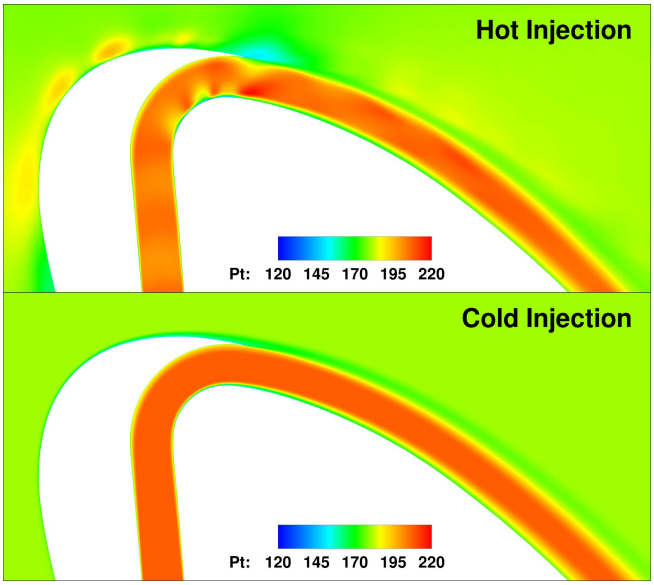

Figure 25: Total Pressure field comparison

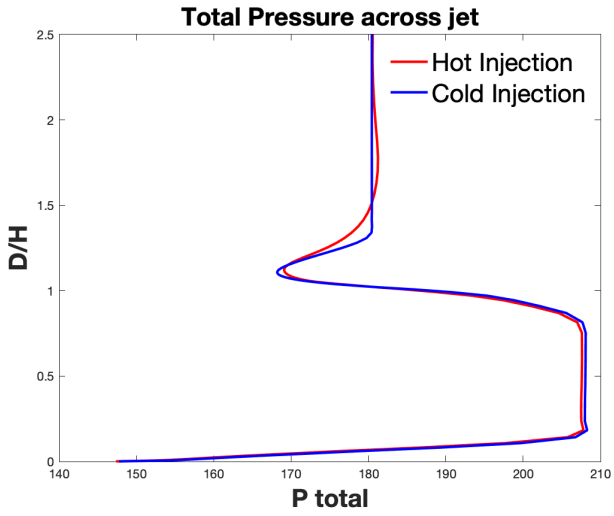

Figure 26: Total Pressure distribution comparison

Figure 27 compares the static pressure fields of the two cases. Just like the total pressure, the comparison between the cases is similar. The most notable difference is the uneven pressure zones on the walls of the injection duct due to the unsteady flow. Figure 28 shows the span-averaged distribution of static pressure across the injection jet. Again, the distributions are nearly identical, with the static pressure being lowest near the wall, increasing linearly across the jet, then increasing more sharply outside of the jet.

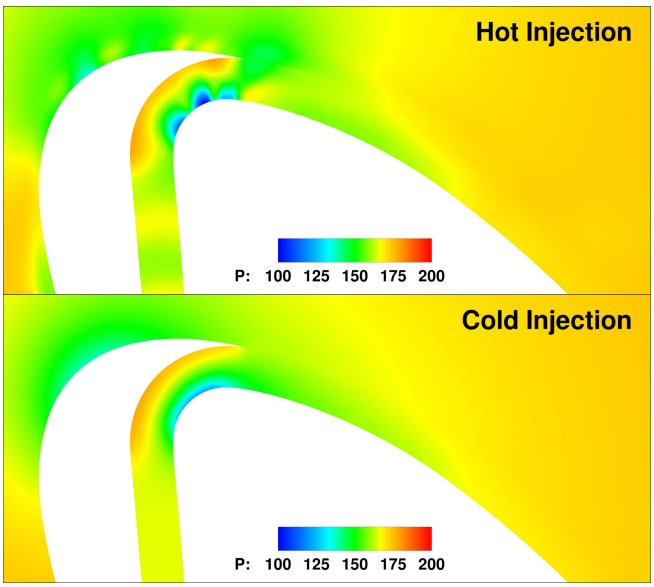

Figure 27: Static Pressure field comparison

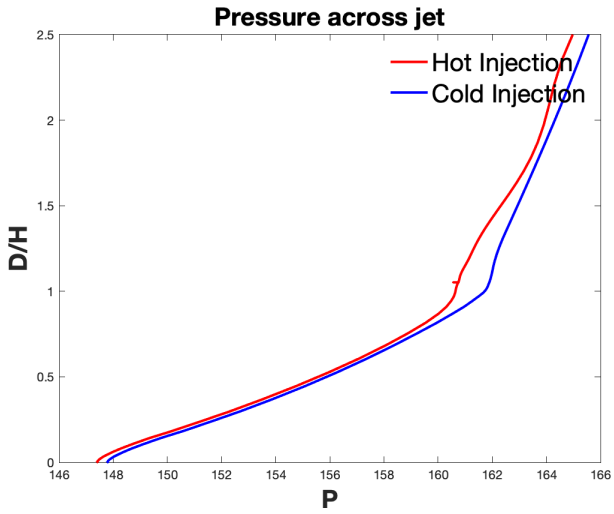

Figure 28: Static Pressure distribution comparison

Figure 29 compares the static temperature fields of the two cases. Like the total temperature, the injection jet of the Hot case has a much higher static temperature than the Cold case. In fact, the Cold case's injection jet temperature is actually lower than the freestream pressure because of its uniform total temperature, but low static pressure. Figure 30 shows the span-averaged distribution of static temperature across the injection jet. Again, the comparison of the distributions is similar to those of the total temperature, where the Hot case has a higher temperature in the jet, but is about the same outside of the jet. The "spikes" in the distribution of each are due to an increase in static temperature due to viscous shear in the boundary layer.

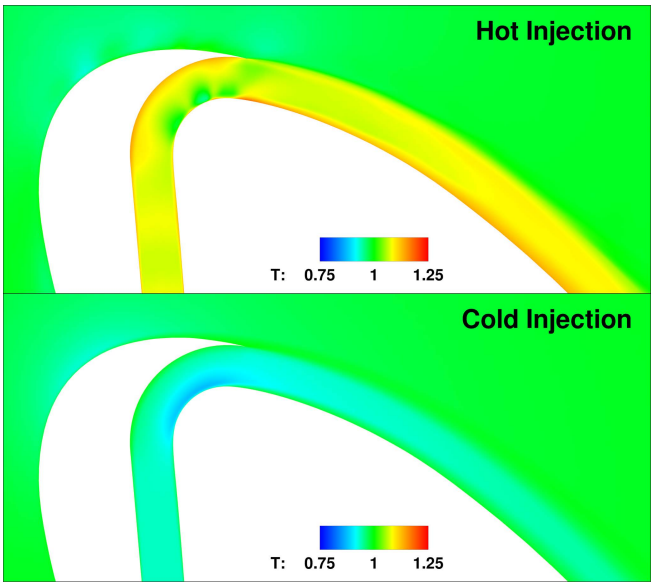

Figure 29: Static Temperature field comparison

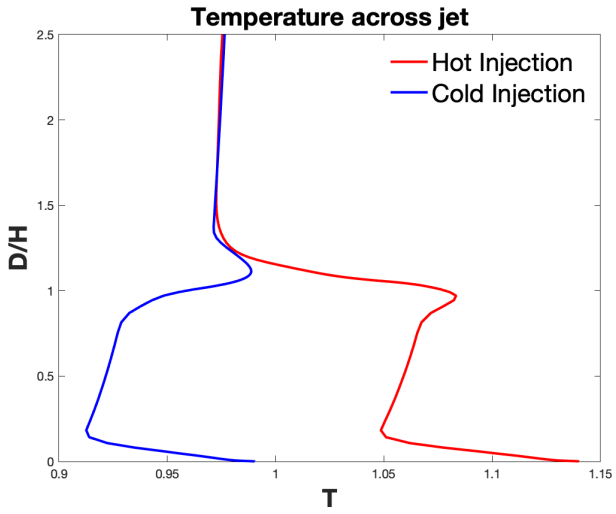

Figure 30: Static Temperature distribution comparison

Figure 31 compares the density fields. The Hot Jet case has a lower injection jet density than the Cold Jet case due to the higher static temperature and unchanged static pressure. These terms are related by the fluid state equation, $\rho = P/RT$. Figure 32 shows the span-averaged distribution of density across the injection jet.

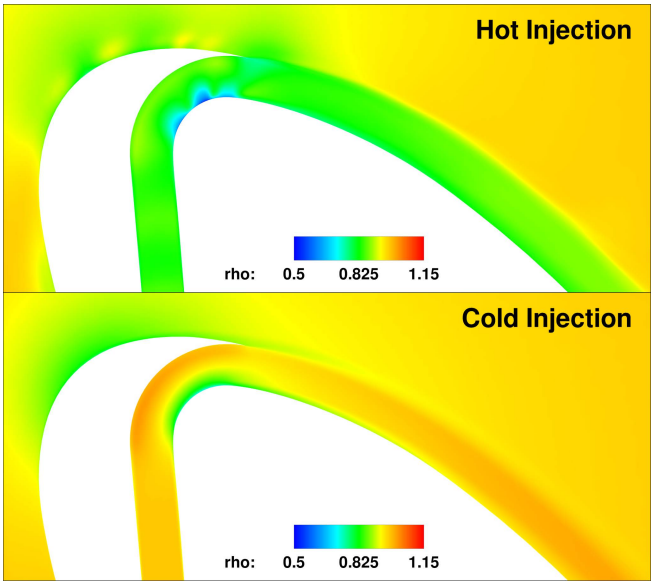

Figure 31: Density field comparison

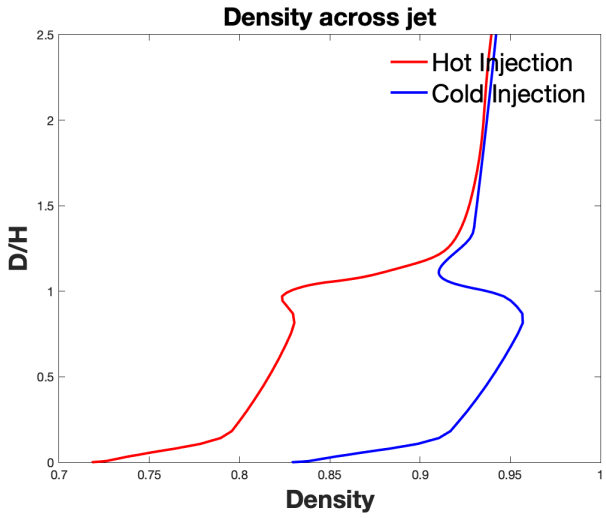

Figure 32: Density distribution comparison

Figure 33 shows the span-averaged distribution of streamwise velocity across the injection jet. The Hot case has a higher injection jet velocity than the Cold case. Again, this relates to the C_μ iteration process. In order to maintain the target injection jet momentum, C_μ, if the fluid density decreases, the velocity much increase. This delta in velocity is also reflected in the differences in stagnation, or "total" values for pressure, temperature, and enthalpy between the two cases: i.e. $P_t = P + u^2/2$.

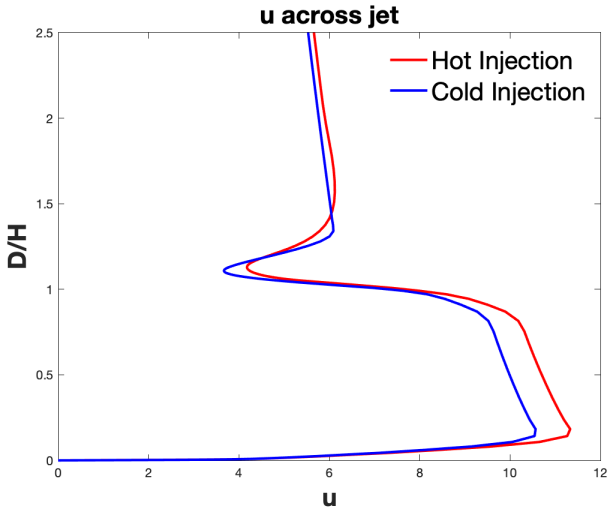

Figure 33: Velocity distribution comparison

3.4 Aerodynamic Forces

Table 2 presents a comparison of the time-averaged aerodynamic results of the two 3D IDDES CFJ cases studied, and the baseline NACA6421 airfoil at its maximum lift condition, also simulated with 3D IDDES [3]. Compared to the previously studied CFJ airfoil case with constant total enthalpy micro-compressor efficiency and the same flow conditions, the present study shows a 4.7% increase in lift, but a 286% increase in drag and 56% increase in power required. The 34% drop in the corrected aerodynamic efficiency is primarily attributed to the increase in the power coefficient. However, simply dividing the P_c of the Cold Jet case by 70% should yield an $(C_L/C_D)_c$ of 1.885, which is higher than the resulting $(C_L/C_D)_c$ for the $\eta = 70\%$ Hot Jet case. This 0.101 (5.7%) difference in corrected aerodynamic efficiency must be attributed to the additional pumping power required due to entropy losses and a higher injection total temperature. The Hot case's injection jet and wall jet shear layer are considerably more turbulent, and the time averaged net drag is 3.86 times greater than the Cold case. The power required is the dominant factor in the denominator of the corrected aerodynamic efficiency, $(C_L/C_D)_c = C_L/(C_D + P_c)$. The P_c term makes up 99.2% of the denominator for the Cold case, and 98.1% of the denominator for the Hot case.

Table 2: Time-Averaged Aerodynamic Coefficients of 3D CFJ and Baseline Airfoils

Case	C_μ	C_L	C_D	P_C	C_L/C_D	$(C_L/C_D)_c$	Inj Ma
3D CFJ Hot Jet	2.5	10.036	0.108	5.516	92.720	1.784	0.854
3D CFJ Cold Jet	2.5	9.583	0.028	5.056	343.305	1.885	0.850
3D Baseline 6421	-	1.514	0.105	-	14.433	14.433	-

Table 3 presents the total pressure and temperature values at the inlet and outlet of the CFJ compressor. PTR is the total pressure ratio across the compressor, P_{01}/P_{02}, and TTR is the total temperature ratio across the compressor, T_{01}/T_{02}. The Cold case has a slightly higher injection total pressure, but the total pressure ratio is similar between the two cases. The injection total temperature of the Cold case is about the same as the freestream, but the T_t of the Hot case is 19.6% higher. For reference, if the freestream temperature is 80°F, the CFJ injection would be 187°F. While the injection jet temperature is drastically higher, the total temperature ratio, TTR, is only about 1.034, which is only a bit higher than the TTR expected when considering the isentropic pressure ratio relation (Eq. 29). The hot flow exiting the CFJ injection jet does mix with the external flow, but only transfers a fraction of its energy, so the flow ingested by the compressor through the suction duct is still 15.7% higher T_t than the freestream total temperature. At this injection total temperature, the heat generated by the efficiency losses of the compressor are in equilibrium with the heat transfer across the jet mixing layer.

Table 3: CFJ Compressor Parameters of 3D CFJ Airfoils

Case	$P_t\ Inj$	$P_t\ Suc$	$T_t\ Inj$	$T_t\ Suc$	PTR	TTR
Hot Jet	206.619	191.544	1.196	1.157	1.079	1.034
Cold Jet	207.096	192.465	1.001	0.999	1.076	1.002

The P_t and T_t values in Table 3 are calculated as the mass-flow-rate-weighted average at a position inside the duct 5 cells away from the inlet/outlet boundary condition, to avoid the numerical dispersion effects of the boundary index itself. The method for numerically integrating a MFR-weighted average is given in Eq. 44, with ϕ as the averaged variable. Figures 34–37 show where these values were calculated, and show example slices of the Cold Jet case's flow field at those points. Note how the injection flow of Figs. 34–35 is very 2-dimensional, while the suction flow of Figs. 36–37 is 3-dimensional due to the highly turbulent flow around the suction duct.

$$\frac{\int \phi\rho|\mathbf{V}\cdot d\mathbf{A}|}{\int \rho|\mathbf{V}\cdot d\mathbf{A}|} = \frac{\sum_{i=1}^{n} \phi\rho_i|\mathbf{V}_i\cdot\mathbf{A}_i|}{\sum_{i=1}^{n} \rho_i|\mathbf{V}_i\cdot\mathbf{A}_i|} \tag{44}$$

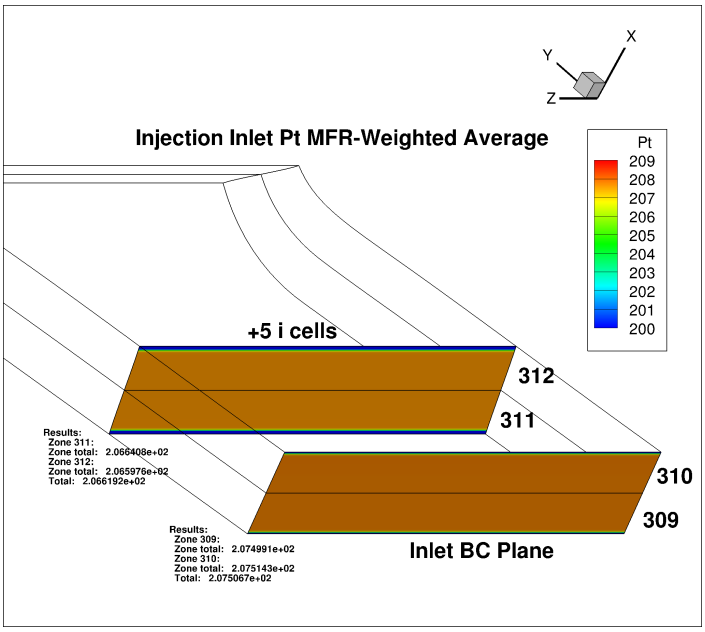

Figure 34: Injection duct P_t integration plane, Cold

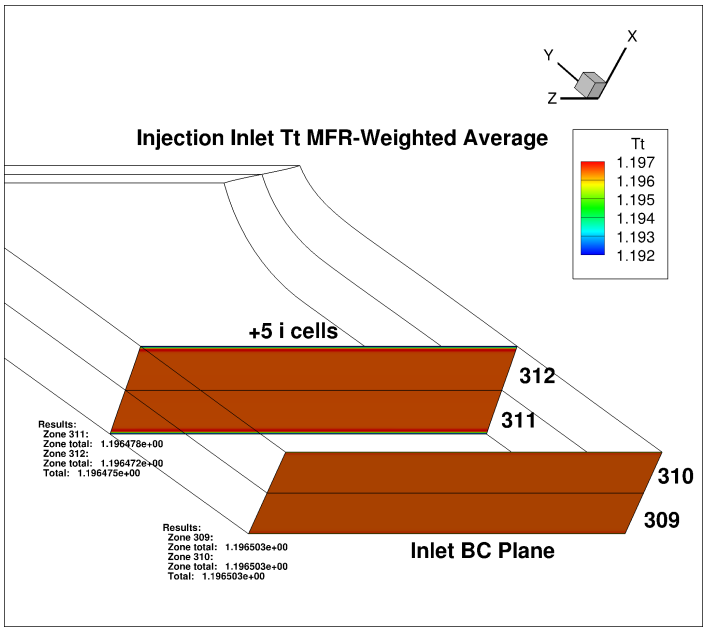

Figure 35: Injection duct T_t integration plane, Cold

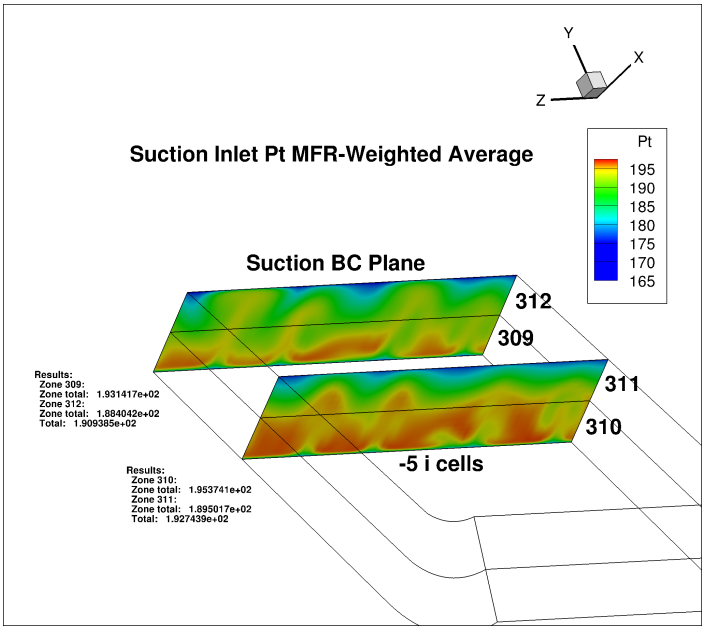

Figure 36: Suction duct P_t integration plane, Cold

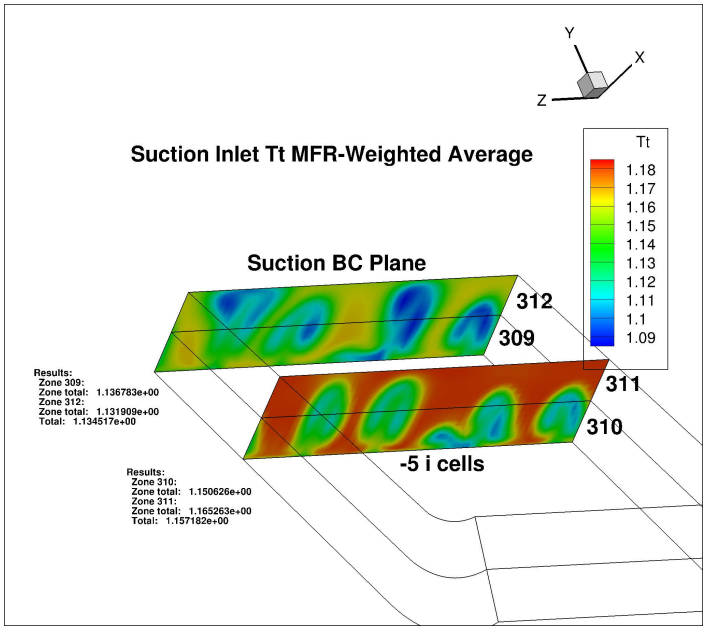

Figure 37: Suction duct T_t integration plane, Cold

Figure 38 displays how the lift coefficient, drag coefficient, power coefficient, and pressure ratio vary in time. For the Cold Jet case, the total lift and drag forces regularly oscillate in time with a reduced frequency of $\bar{f} = 37.04$, corresponding to the shedding frequency of the Kelvin-Helmholtz free shear layer instability [3]. The Hot Jet case does not exhibit regular oscillations; the aerodynamic force history appears more random. The time-averaged coefficients are taken as the average value over the final characteristic time of the simulation. For clarity, the plots for the Hot Jet case show a trailing average as the red line.

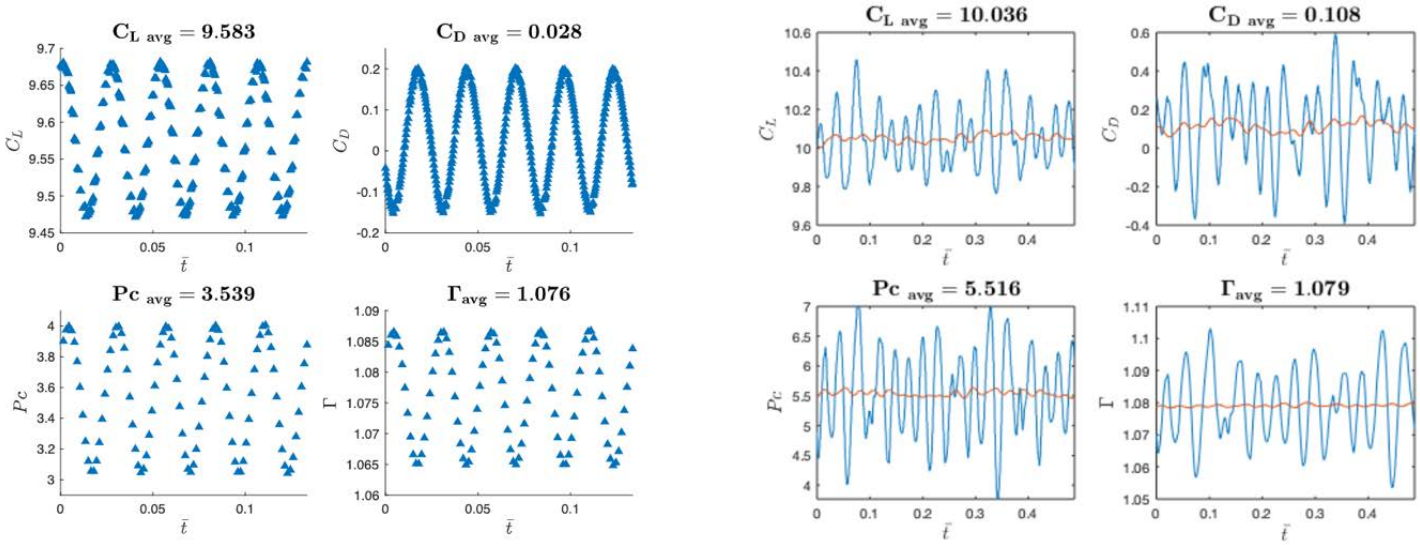

Figure 38: Aerodynamic coefficients in time.
Cold Jet case (Left). Hot Jet case (Right).

Table 4 lists the differences in the mass flow properties between the injection jet flows of each case. Due to the hotter state of the injection jet, the density is proportionally lower. The higher static temperature increases the speed of sound ($a = \sqrt{\gamma RT}$), which allows for a higher flow velocity at the same Mach number. The Hot Jet case has a higher jet velocity but lower mass flow rate, while the Cold Jet case has a lower jet velocity but higher mass flow rate. The injection jet momentum is identical between the two cases.

Table 4: CFJ Injection Jet Characteristics

Case	C_μ	Inj Mach	$\dot{m}$	v_{jet}	ρ
Hot Jet	2.50	0.854	0.0121	10.333	0.834
Cold Jet	2.50	0.850	0.0133	9.443	1.000

Tables 5 & 6 present the factors which contribute to the net lift and drag coefficients. Refer to equations 34 & 35 for details about how each value contributes to the total. The numbers presented for each case are not directly comparable, because they are taken as instantaneous values from unsteady flow fields. These instances were selected to be close to the time-averaged values. On a qualitative basis, the Hot Jet case shows a higher pressure lift, but lower jet F_y. It has a much higher pressure drag, and nearly identical jet F_x.

Table 5: Contributions to C_L (Instantaneous)

Case	Hot	Cold
Surface Pressure - y	15.325	15.213
Surface Shear - y	0.071	-0.089
Surface Force R'_y	15.395	15.124
Inj Jet Pressure - y	1.432	1.440
Suc Jet Pressure - y	-5.857	-5.874
Inj Jet Momentum - y	0.214	0.212
Suc Jet Momentum - y	-1.162	-1.244
Resultant Jet Force $F_{y_{cfj}}$	-5.372	-5.466
Net C_L	10.023	9.659

Table 6: Contributions to C_D (Instantaneous)

Case	Hot	Cold
Surface Pressure - x	15.666	15.207
Surface Shear - x	-0.085	0.070
Surface Force R'_x	15.581	15.277
Inj Jet Pressure - x	-4.420	-4.443
Suc Jet Pressure - x	-7.500	-7.519
Inj Jet Momentum - x	-2.607	-2.604
Suc Jet Momentum - x	-0.899	-0.848
Resultant Jet Force $F_{x_{cfj}}$	-15.424	-15.414
Net C_D	0.157	-0.138

4 Turbulent Kinetic Energy Evaluation

In this section, we compare the two CFJ cases on the basis of their unsteady flow field turbulent kinetic energy (TKE). Evaluating the TKE is especially useful for characterizing and quantifying turbulence within the flow field. TKE is a representation of the energy associated with turbulent fluctuations in the fluid, a key parameter describing the nature of turbulent flows. By contrasting these two CFJ cases in terms of TKE, we gain valuable insights into the interplay between the energy of the injection jet and turbulence generation, making clear the implications of these factors for enhancing the aerodynamic performance of the Co-Flow Jet system. This evaluation allows us to better understand the impact of the higher injection enthalpy, and to assess its potential for advancing real CFJ active flow control strategies.

The turbulent kinetic energy per unit mass is calculated according to Eq. 45. The TKE is half the sum of the mean squared fluctuations in the three velocity components (u', v', and w'). These velocity fluctuations represent how the velocity at a given point differs from the mean velocity in each coordinate direction. Eq. 46 defines the mean squared velocity fluctuations ($\overline{(\mathbf{u}')^2}$) as the integral of the squared difference between the instantaneous velocity, $\mathbf{u}(t)$, and the time-averaged velocity, $\bar{\mathbf{u}}$ over a specified time interval, which quantifies the variance of the kinetic energy associated with the turbulent fluctuations of the velocity field. For the Cold Jet case, the time-averaged velocity field was calculated using the final 20 periods, sampling the flow field every $0.0006\tilde{t}$. For the Hot Jet case, the time-averaged velocity field was calculated using the final $1.0\tilde{t}$, sampling every $0.0006\tilde{t}$.

$$TKE = \frac{1}{2}\left(\overline{(u')^2} + \overline{(v')^2} + \overline{(w')^2}\right) \tag{45}$$

$$\overline{(\mathbf{u}')^2} = \frac{1}{T}\int_{T_1}^{T_2} (\mathbf{u}(t) - \bar{\mathbf{u}}))^2 dt \tag{46}$$

Figure 39 shows instantaneous TKE fields for each case, focused on the airfoil leading edge and injection region. The Hot case shows orders of magnitude higher TKE than the Cold case (note the scale in the bottom right of the figures). The Cold case has a steady, stable injection flow, while the Hot case is very unsteady. The additional enthalpy introduced by the CFJ injection boundary introduces the baroclinic instability throughout the jet, leading to its unsteady nature.

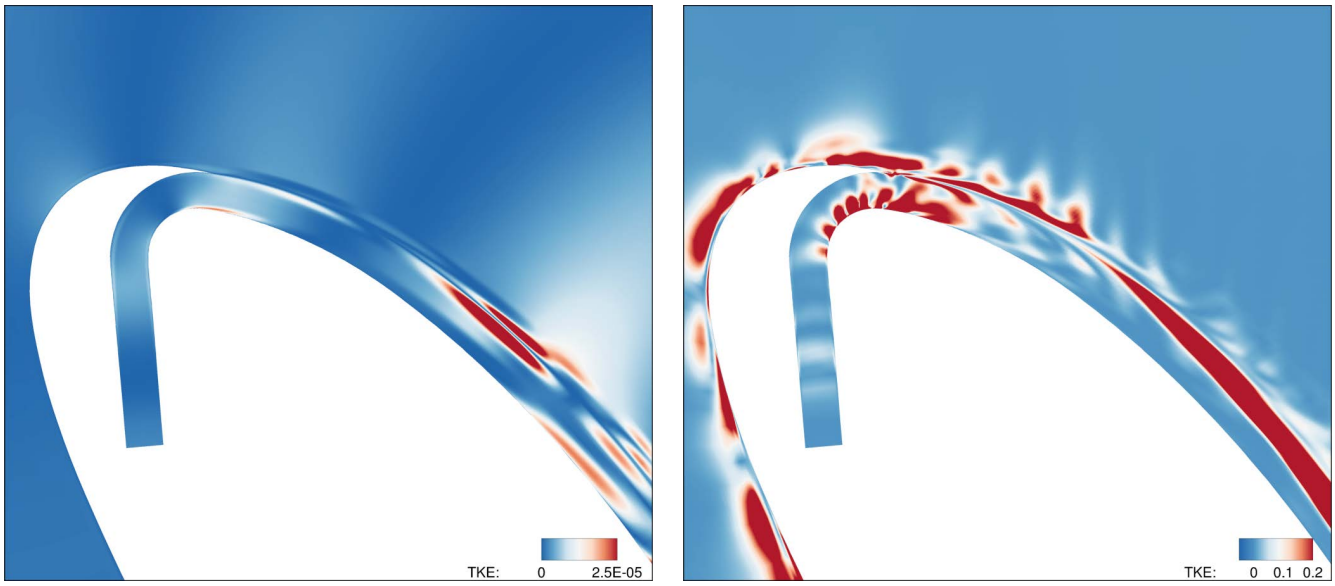

Figure 39: Inst. TKE fields of CFJ injection duct and LE.
Cold Jet case (Left). Hot Jet case (Right).

Fig. 40 focuses on the TKE field around the suction duct and tail of the CFJ airfoil. The flow field is noticeably more turbulent in this region. Local regions of high TKE occur at the fast-moving center of vortex tubes. The Cold case shows vortex tubes forming in the shear layer at regular intervals, and rolling down the tail surface at the same frequency. The Hot case is much more turbulent. The shear layer vortex sheet is less organized, and begins farther upstream. Unlike the more organized Cold Jet case's flow field, there is no discernible periodicity of the vortex shedding within the shear layer, or from the trailing edge of the airfoil. This is reflected in the seemingly random aerodynamic force history shown in Fig. 38 (Right).

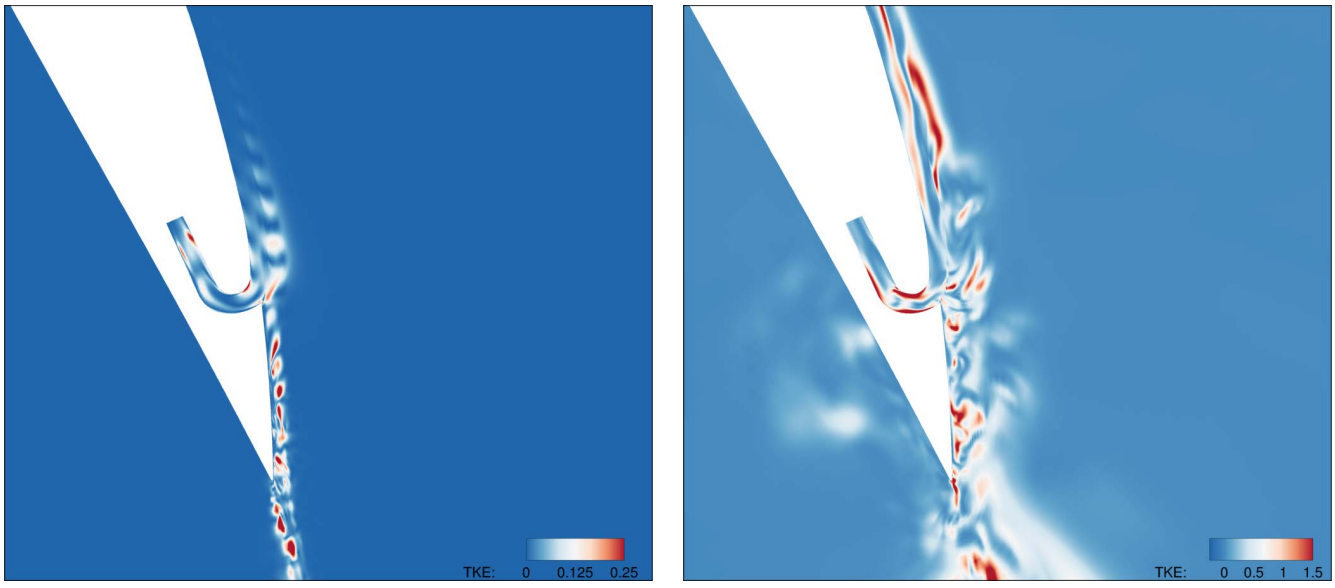

Figure 40: Inst. TKE fields of CFJ suction duct and tail.
Cold Jet case (Left). Hot Jet case (Right).

5 Conclusions

This study pioneers the investigation into the effects of Hot Jet Co-Flow Jet active flow control, whereas past research has used Cold Jet CFJ. By considering thermodynamic conditions closer to reality, the analysis provides valuable insights into the performance and operation of future real CFJ airfoils. The Hot Jet shows much higher turbulence and unsteady behavior compared to the Cold Jet. This significantly greater turbulence is found to be due to the higher total enthalpy, and total enthalpy gradient of the injection flow, leading to complex vortical flow in the injection duct. The vorticity of the Hot Jet's injection flow improves mixing between the wall jet and the external flow, helping to transfer more energy and momentum from the wall jet to the main flow, which enhances the airfoil's performance. This Hot Jet CFJ airfoil case sustains attached, lifting flow at $\alpha = 65°$, producing a net $C_L = 10.04$, 4.8% greater than its Cold Jet CFJ counterpart. That improvement to the lift coefficient comes at the expense of a greater drag and 9.1% increase in power required. For a compressor efficiency of 70%, we expected a 5.7% higher airfoil aerodynamic efficiency. This difference must derive from the effects of entropy on this highly turbulent flow system. This finding implies that real CFJ applications likely require a somewhat greater power, and have a somewhat lower aerodynamic efficiency than previous studies have reported. The degree of this difference is a topic of future research. This study is a high C_μ "edge case" application of the CFJ. Most other CFJ applications likely have more mild gradients and perform closer to ideal than this case.

This research demonstrates the effects of a Hot Jet in CFJ active flow control, providing a more realistic view of its physical and operational dynamics. The findings highlight improved lift performance and the associated power requirements, offering a more thorough understanding of the flow physics. By advancing the our understanding of Hot Jet CFJ, this study supports further maturity of CFJ technology, contributing to its ongoing improvement and effectiveness in practical applications.

References

[1] "Pack, l. g., and joslin, r. d. (1998, june). overview of active flow control at nasa langley research center. in smart structures and materials 1998: Industrial and commercial applications of smart structures technologies (vol. 3326, pp. 202-213). spie.."

[2] "Jahanmiri, m. (2010). active flow control. a review.."

[3] B. McBreen, Y.-C. Yang, and G.-C. Zha, "Improved Delayed Detached Eddy Simulation of Co-Flow Jet Flow Control in Extreme Adverse Pressure Gradients." AIAA Paper 2024-0063, AIAA SciTech 2024 Forum. Orlando, FL., Jan 2024.

[4] Yang, Y.-C. and Zha, G.-C., "Super-Lift Coefficient of Active Flow Control Airfoil: What Is the Limit?." AIAA Paper 2017-1693, AIAA SCITECH2017, 55th AIAA Aerospace Science Meeting, Grapevine, Texas, 9-13 January 2017.

[5] G.-C. Zha, Y.-C. Yang, Y. Ren, and B. McBreen, "Super-lift and thrusting airfoil of coflow jet-actuated by micro-compressors." AIAA Paper 2018-3061, AIAA AVIATION 2018, Atlanta, GA , 25 - 29 June 2018.

[6] Zha, G.-C and Carroll, B. and Paxton, C. and Conley, A. and Wells, A., "High Performance Airfoil with Co-Flow Jet Flow Control," *AIAA Journal*, vol. 45, 2007.

[7] Lefebvre, A. and Dano, B. and Bartow, W. and Di Franzo, M. and Zha, G.-C., "Performance and Energy Expenditure of Co-Flow Jet Airfoil with Variation of Mach Number," *AIAA Journal of Aircraft*, vol. 53, pp. 1757–1767, 2016.

[8] K.-W. Xu, Y. Ren, and G.-C. Zha, "Flow separation control by coflow wall jet." Proceedings of AIAA Aviation 2021, Aug. 2-6, 2021, Submitted to AIAA Journal, 2-6 Aug. 2021.

[9] G.-C. Zha and D. C. Paxton, "A Novel Flow Control Method for Airfoil Performance Enhancement Using Co-Flow Jet." *Applications of Circulation Control Technologies*, Chapter 10, p. 293-314, Vol. 214, Progress in Astronautics and Aeronautics, AIAA Book Series, Editors: Joslin, R. D. and Jones, G.S., 2006.

[10] Zha, G.-C. and Gao, W. and Paxton, C., "Jet Effects on Co-Flow Jet Airfoil Performance," *AIAA Journal, No. 6,*, vol. 45, pp. 1222–1231, 2007.

[11] K.-W. Xu and G.-C. Zha, "High control authority 3d aircraft control surfaces using co-flow jet," *AIAA Journal of Aircraft*, July 2020.

[12] Xu, Kewei and Ren, Yan and Zha, Gecheng, "Numerical Analysis of Energy Expenditure for Co-Flow Wall Jet Separation Control ," *AIAA Journal*, vol. 60, no. 5, p. doi.org/10.2514/1.J061015, 2022.

[13] Lefebvre, A. and Zha, G.-C., "Trade Study of 3D Co-Flow Jet Wing for Cruise and Takeoff/Landing Performance." AIAA Paper 2016-0570, AIAA SCITECH2016, AIAA Aerospace Science Meeting, San Diego, CA, 4-8 January 2016.

[14] P. Barrios, Y. Ren, and G.-C. Zha, "Simulation of 3d co-flow jet airfoil with integrated micro-compressor actuator at different cruise mach numbers." AIAA Paper-2023-2118, AIAA SCITECH 2023 Forum, 23 Jan, 2023.

[15] "Ge-cheng zha, " feasibility study of deflected slipstream airfoil for vtol hover enabled by coflow jet ", aiaa paper-2023-4279, aiaa aviation 2023 forum, 12-16 june 2023, san diego, ca."

[16] B. McBreen, E. Butler, and G.-C. Zha, "Analysis of Wall Jet Flow in EAPG with Super-Lift Coefficient." Proceedings of AIAA Scitech 2024. Orlando, FL., Jan 2024.

[17] B. McBreen, K.-W. Xu, and G.-C. Zha, "Numerical Study of Extreme Adverse Pressure Gradients Enabled by Co-Flow Jet." AIAA Paper 2023-1430, AIAA SciTech Forum, National Harbor, MD, 23-27 January, 2023.

[18] Y. Wang, Y.-C. Yang, and G.-C. Zha, "Study of Super-Lift Coefficient of Co-Flow Jet Airfoil and Its Power Consumption." AIAA Paper 2019-3652, AIAA Aviation 2019, AIAA Applied Aerodynamics Conference, Dallas, Texas, 17-21 June 2019.

[19] K. Xu and G. Zha, "Investigation of coflow jet active flow control for wind turbine airfoil." AIAA 2020-2942, 2020 AIAA AVIATION Forum and Exposition, Virtual Event, 15-19 June, 2020.

[20] K.-W. Xu and G.-C. Zha, "High efficiency wind turbine using co-flow jet active flow control." ASME Paper GT2021-59664, Proceedings of ASME Turbo Expo 2021 Turbomachinery Technical Conference and Exposition, Virtual, Online, June 07-11, 2021.

[21] "Yan ren, kewei xu, and gecheng zha, "wind turbine effciency enhancement by coflow jet airfoil", aiaa paper 2022-1787, aiaa scitech forum, january 3-7, 2022, san diego, ca."

[22] "Yan ren, gecheng zha, nick johnson, ganesh vijayakuma, "high efficiency 2-bladed utility wind turbine enhanced by coflow jet active flow control", aiaa paper-2023-0608, aiaa scitech 2023 forum, 23-27 january 2023, national harbor, md."

[23] "Yang wang, gecheng zha, alexis lefebvre, "study of mach number effect on cruise efficiency for a co-flow jet general aviation airplane", paper 2021-1303, aiaa scitech forum, 11–15; 19–21 january 2021, virtual event."

[24] "Zhixiang liu, gecheng zha, "transonic airfoil performance enhancement using co-flow jet active flow control", aiaa paper 2016-3472, aiaa aviation 2016, 8th aiaa flow control conference, washington, d.c., 13-17 june 2016."

[25] "Paula a. barrios, yan ren, gecheng zha, " simulation of 3d co-flow jet airfoil control with micro-compressor actuator at high angles of attack ", aiaa paper-2023-4208, aiaa aviation 2023 forum, 12-16 june 2023, san diego, ca."

[26] Wang, B.-Y. and Haddoukessouni, B. and Levy, J. and Zha, G.-C., "Numerical Investigations of Injection Slot Size Effect on the Performance of Co-Flow Jet Airfoil ," *AIAA Journal of Aircraft*, vol. 45, pp. 2084–2091, 2008.

[27] P. Spalart and S. Allmaras, "A One-equation Turbulence Model for Aerodynamic Flows." AIAA-92-0439, 1992.

[28] Y.-C. Yang and G.-C. Zha, "Simulation of airfoil stall flows using iddes with high order schemes." AIAA Paper 2016-3185, AIAA AVIATION 2016, 46th AIAA Fluid Dynamics Conference, Washington, D.C., 13-17 June 2016 , 2016.

[29] Yang, Y.-C. and Fernandez, M. and Zha, G.-C., "Improved Delayed Detached Eddy Simulation of Super-Lift Flow of Co-Flow Jet Airfoil." AIAA Paper 2018-0314, AIAA SciTech Forum, 2018 AIAA Aerospace Sciences Meeting, Kissimmee, FL, 8-12 January 2018.

[30] A. Jameson, "Time Dependent Calculations Using Multigrid with Applications to Unsteady Flows Past Airfoils and Wings." AIAA Paper 91-1596, 1991.

[31] Shen, Y.-Q. and Zha, G.-C. and Wang, B.-Y., " Improvement of Stability and Accuracy of Implicit WENO Scheme," *AIAA Journal*, vol. 47, No. 2, pp. 331–344, 2009.

[32] Shen, Y.-Q. and Zha, G.-C. and Chen, X.-Y., " High Order Conservative Differencing for Viscous Terms and the Application to Vortex-Induced Vibration Flows," *Journal of Computational Physics*, vol. 228(2), pp. 8283–8300, 2009.

[33] Shen, Y.-Q. and Zha, G.-C. , " Improvement of the WENO Scheme Smoothness Estimator," *International Journal for Numerical Methods in Fluids*, vol. 64, p. DOI:10.1002/fld.2186, 2010.

[34] G.-C. Zha, Y. Shen, and B. Wang, "An improved low diffusion E-CUSP upwind scheme ," *Journal of Computer & Fluids*, vol. 48, pp. 214–220, 2011.

[35] G.-C. Zha and E. Bilgen, "Numerical Solutions of Euler Equations by Using a New Flux Vector Splitting Scheme," *International Journal for Numerical Methods in Fluids*, vol. 17, pp. 115–144, 1993.

[36] G.-C. Zha and E. Bilgen, "Numerical Study of Three-Dimensional Transonic Flows Using Unfactored Upwind-Relaxation Sweeping Algorithm," *Journal of Computational Physics*, vol. 125, pp. 425–433, 1996.

[37] B.-Y. Wang and G.-C. Zha, "A General Sub-Domain Boundary Mapping Procedure For Structured Grid CFD Parallel Computation," *AIAA Journal of Aerospace Computing, Information, and Communication*, vol. 5, No.11, pp. 2084–2091, 2008.

[38] Xu, Kewei and Zha, Gecheng, "System energy benefit using co-flow jet active separation control for a serpentine duct," *Elsevier Journal of Aerospace Science and Technology*, vol. 128, p. DOI: 10.1016/j.ast.2022.107746, 2022.

[39] Wang, B. Y and Zha, G.-C., " Detached-Eddy Simulation of a Co-Flow Jet Airfoil at High Angle of Attack ," *AIAA Journal of Aircraft*, vol. 48, pp. 1495–1502, 2011.

[40] Im, H.-S. and Zha, G.-C. and Dano, B. P. E., "Large Eddy Simulation of Coflow Jet Airfoil at High Angle of Attack," *Journal of Fluid Engineering*, vol. 136(2), p. 021101, 2014.

[41] Y.-Q. Shen and G.-C. Zha, "Large Eddy Simulation Using a New Set of Sixth Order Schemes for Compressible Viscous Terms ," *Journal of Computational Physics*, vol. 229, pp. 8296–8312, 2010.

[42] M. Minervino and R. Tognaccini, "A unified thermodynamic/lamb-vector-based analysis of the aerodynamic force," *Physics of Fluids https://doi.org/10.1063/5.0164384*, vol. 35, 2023.

[43] E. Greitzer, "Internal Flow: Concepts and Aplications." Cambridge University Press, 2004.